AGU PUBLICATIONS

JGR

Journal of Geophysical Research: Solid Earth

RESEARCH ARTICLE
10.1002/2017JB014465

Key Points:
- The most complete and up-to-date velocity field in the India-Eurasia collision zone including 2576 GPS stations observed from 1991 to 2015
- Velocity field shows several large undeforming areas, strain around some major faults, areas of diffuse strain, and dilation of high plateau
- There was no robust evidence for discrepancy between geological and geodetic slip rates of the major strike-slip faults in Tibet

Supporting Information:
- Data Set S1
- Figures S1–S7

Correspondence to:
H. Wang, Y. Lou, and R. Zhang,
ehwang@163.com;
ydlou@whu.edu.cn;
rzhang@neis.cn

Citation:
Zheng, G., Wang, H., Wright, T. J., Lou, Y., Zhang, R., Zhang, W., … Wei, N. (2017). Crustal deformation in the India-Eurasia collision zone from 25 years of GPS measurements. *Journal of Geophysical Research: Solid Earth*, *122*, 9290–9312. https://doi.org/10.1002/2017JB014465

Received 24 MAY 2017
Accepted 17 SEP 2017
Accepted article online 21 SEP 2017
Published online 6 NOV 2017

Crustal Deformation in the India-Eurasia Collision Zone From 25 Years of GPS Measurements

Gang Zheng[1,2], Hua Wang[2,3], Tim J. Wright[4], Yidong Lou[1,2], Rui Zhang[5], Weixing Zhang[1], Chuang Shi[1,2], Jinfang Huang[1], and Na Wei[1]

[1]GNSS Research Center, Wuhan University, Wuhan, China, [2]Collaborative Innovation Center of Geospatial Technology, Wuhan University, Wuhan, China, [3]Department of Surveying Engineering, Guangdong University of Technology, Guangzhou, China, [4]COMET, School of Earth and Environment, University of Leeds, Leeds, UK, [5]National Earthquake Infrastructure Service, China Earthquake Administration, Beijing, China

Abstract The India-Eurasia collision zone is the largest deforming region on the planet; direct measurements of present-day deformation from Global Positioning System (GPS) have the potential to discriminate between competing models of continental tectonics. But the increasing spatial resolution and accuracy of observations have only led to increasingly complex realizations of competing models. Here we present the most complete, accurate, and up-to-date velocity field for India-Eurasia available, comprising 2576 velocities measured during 1991–2015. The core of our velocity field is from the Crustal Movement Observation Network of China-I/II: 27 continuous stations observed since 1999; 56 campaign stations observed annually during 1998–2007; 1000 campaign stations observed in 1999, 2001, 2004, and 2007; 260 continuous stations operating since late 2010; and 2000 campaign stations observed in 2009, 2011, 2013, and 2015. We process these data and combine the solutions in a consistent reference frame with stations from the Global Strain Rate Model compilation, then invert for continuous velocity and strain rate fields. We update geodetic slip rates for the major faults (some vary along strike), and find that those along the major Tibetan strike-slip faults are in good agreement with recent geological estimates. The velocity field shows several large undeforming areas, strain focused around some major faults, areas of diffuse strain, and dilation of the high plateau. We suggest that a new generation of dynamic models incorporating strength variations and strain-weakening mechanisms is required to explain the key observations. Seismic hazard in much of the region is elevated, not just near the major faults.

1. Introduction

1.1. Continental Deformation and the India-Eurasia Collision

The India-Eurasia collision zone is the largest deforming region on the planet (Molnar & Tapponnier, 1975). The collision initiated at ~59 ± 1 Ma (Hu et al., 2016), with the continuing northward motion of India since has created a region of deformed lithosphere that reaches from the Himalayan front to the Mongolia Steppe. Active deformation resulting from the convergence is readily observable, for example, in surface topography (Fielding et al., 1994), crustal thickness (Li et al., 2014), lithospheric thickness (McKenzie & Priestley, 2008), seismicity (Priestley et al., 2008), and geodetic strain rates (Kreemer et al., 2014).

Any successful model that attempts to explain how the continents deform must be able to explain observations of deformation in the India-Eurasia collision zone—the region has therefore long been the focus for heated debates around competing hypotheses for continental tectonics. For tectonic geodesists, the central debate has typically been framed, for example, by Thatcher (1995, 2009), as a contrast between microplate and continuum models, with geodetic data often invoked to test these models.

In the "microplate/block model" approach, the continents are divided into a number of rigid plates, each obeying the kinematic rules of plate tectonics (McKenzie & Parker, 1967), that the velocities at any point in the block can be described by rotations around an Euler pole with strain only occurring around the boundaries of the blocks. To predict the surface deformation for a region using a microplate model, we need to define the boundaries of each discrete microplate/block, their Euler poles, and their rotation velocities. In addition, deformation caused by elastic strain accumulation around the block boundaries can be included (McCaffrey, 2002). Avouac and Tapponnier (1993) proposed the first microplate model for the India-Eurasia collision. This model consisted of four microplates (Siberia, Tarim, Tibet, and India), with the relative velocities

and rotation rates constrained by the available geological estimates of slip rates on the major faults separating these blocks. As geodetic data from Global Navigation Satellite Systems such as the Global Positioning System (GPS) became available in increasing numbers, these models have become more complex, with increasing numbers of blocks required to explain the data. For example, to explain the velocities of ~45 GPS sites in Tibet, Chen et al. (2004) also used four blocks but required internal deformation within those blocks; Thatcher (2007) used 11 blocks to explain the 349 GPS velocities; and Loveless and Meade (2011) required 24 blocks to describe the motion of 731 GPS sites, and significant internal deformation was still required in many of the blocks, particularly those in the Tibetan Plateau. Most recently, Wang, Qiao, et al. (2017) were able to fit 1854 GPS velocities with a 30-block model. Although they obtained a mean residual (1.08 mm/yr) that was smaller than the mean uncertainty in the observations (1.36 mm/yr), they still had significant regional residuals in southern and south-eastern Tibet.

In the "continuum model" approach, physical laws are used to determine the surface velocities of a deforming region, most typically by considering the lithosphere to deform as if it was a viscous fluid (England & McKenzie, 1982). To predict the surface deformation from such a model requires information about the forces acting on the boundary, the internal forces arising from gradients in gravitational potential energy, and knowledge of the rheological properties of the material within the model. England and Houseman (1986) proposed the first continuum model for the India-Eurasia collision, prior to the availability of geodetic constraints. Their model consisted of a thin viscous sheet with uniform effective viscosity, subjected to a rigid indentor representing the Indian plate. Neil and Houseman (1997) adapted this model by including a strong Tarim basin to explain why that region had not experienced crustal thickening and is not deforming at present. As with microplate/block models, additional sophistication has been required in order for such models to explain the ever-improving observations. Flesch et al. (2001) were able to explain 364 GPS velocities and Quaternary slip rates by inverting for spatial variations in effective viscosity across 250 small regions; Lechmann et al. (2011) built a complex model consisting of 3-D variations in viscosity, including strong Tarim and Sichuan basins and weak Chaman and Sagaing Faults and tested this against the 553 GPS velocities presented in Zhang et al. (2004).

In this paper, we attempt to take a step back from this polarizing debate to rigorously assess the latest observations. Our new GPS observations provide the most accurate and dense measurements of deformation for the whole India-Eurasia collision zone to date—we use the data to extract the key features of the deforming zone and test existing models against these. We find that neither block nor continuum models can explain all the observations and suggest that a new generation of models is required.

1.2. Previous GPS Work in the India-Eurasia Collision Zone

GPS geodesy can measure the displacements and velocities of benchmarks with high precision, and these can be combined to produce regional crustal velocity fields (e.g., Freymueller, 2011). Since the 1990s, GPS measurements have been widely used to study crustal deformation in the India-Eurasia collision zone. Wang et al. (2001) for the first time provided a global picture of the continental deformation in China by GPS, presenting the velocities of 354 stations. Following Wang et al. (2001), the density and accuracy of GPS observations have been gradually increased, especially supported by the CMONOC-I/II projects (Crustal Movement Observation Network of China / Tectonic and Environmental Observation Network of Mainland China) (see Figure 1 for the distribution of CMONOC-I/II GPS stations). Subsequently, a number of groups used denser GPS observations to study the crustal deformation in the Tibetan Plateau, such as Zhang et al. (2004) with 553 stations, Gan et al. (2007) with 726 stations, Liang et al. (2013) with 750 stations, Ge et al. (2015) with 1323 stations, and Wang, Qiao, et al. (2017) with 1854 stations. Recently, Li, You, et al. (2012) and Zhao et al. (2015) presented the GPS velocity field for all of China, with measurements made at ~2000 CMONOC-I/II stations. However, these studies were limited by the time span of their GPS data; some published velocities were derived from only two repeated measurements (e.g., ~1000 sites in Li, You, et al. (2012) and 165 sites in Liang et al. (2013)). In addition, some velocity fields included postseismic deformation (e.g., that in Zhao et al., 2015), which might produce significant effects on position time series. Kreemer et al. (2014) compiled a global GPS velocity field, which included velocities in the India-Eurasia collision zone incorporated from 32 studies (see their Appendix A for details), but it was a global study that was not designed for a detailed analysis of the India-Eurasia collision zone.

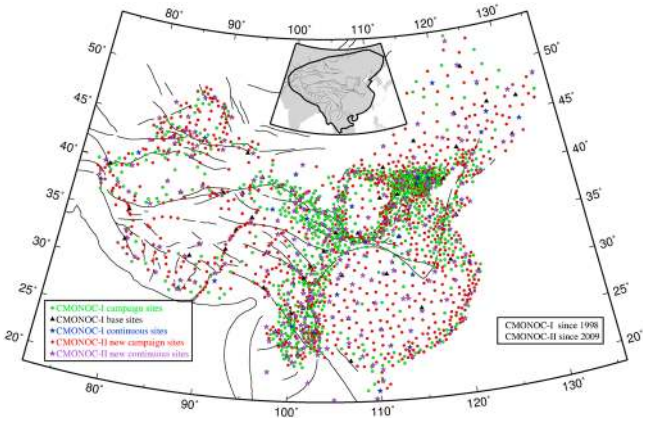

Figure 1. Locations of GPS stations from the CMONOC-I/II projects. The region bounded by the black line in the inset is our study area in the paper.

1.3. Our GPS Data and the Scope of This Paper

We processed all the GPS data collected via the CMONOC-I/II projects up to the end of 2015 and combined these results with the GPS velocities outside the CMONOC-I/II projects presented in Kreemer et al. (2014). As a result, we provide the most complete, accurate, and up-to-date compilation of crustal velocities in the India-Eurasia collision zone with 2576 GPS stations measured between 1991 and 2015. The quality of the data from China has benefited from the increases in number of stations and durations of station occupations, particularly for the CMONOC-II project. Although the data from other surveys in the surrounding countries have in general been presented before, our resultant velocity field in a consistent Eurasia-fixed reference frame is important for studying continental deformation and earthquake hazard in the region.

Based on the GPS velocity field, we estimate the strain distribution and interseismic slip rates of the major faults. Subsequently, we analyze the key features of our new velocity field, including undeforming regions, strain concentrations around some major faults, regions of diffuse deformation, and dilation of the high-elevation regions in Tibet. Then we discuss a series of key questions, including along-strike change in the slip rate, geological versus geodetic slip rate estimates, block versus continuum models, and implications for seismic hazard.

2. GPS Velocity and Strain Rate Fields

2.1. CMONOC-I/II GPS Data Processing

The core part of our velocity field is based on CMONOC-I/II. CMONOC-I contains 27 continuous stations observed since 1999; 56 base stations observed annually from 1998 to 2007 with 8 day occupations; and 1000 campaign stations observed in 1999, 2001, 2004, and 2007 with 4 day occupation in each survey. Since CMONOC-II, the base stations were reformed so that observations were only operated as continuous or campaign mode. Thereafter we have 260 continuous stations since the end of 2010 and 2000 campaign stations observed in 2009, 2011, 2013, and 2015.

We use the PANDA software developed at Wuhan University (Shi et al., 2015) to process the GPS data from CMONOC-I/II in single-day solutions with the Precise Point Positioning mode (Zumberge et al., 1997) (see Table 1 for details). Unlike GIPSY (Webb & Zumberge, 1993) and GAMIT (King & Bock, 1995), which need additional postprocessing steps to obtain constrained positions, PANDA directly provides constrained solutions in the reference frame of the precise ephemeris. In this study, we use precise ephemeris in IGS08 reference frame, which is the IGS realization of International Terrestrial Reference Frame 2008 (Rebischung et al., 2012).

The position time series may be affected by replacement, update, and failure of GPS instruments, as well as coseismic and postseismic deformation of earthquakes. We deal with the instrument issues according to the Station Memorabilia provided by National Earthquake Infrastructure Service of China. We consider all the major earthquakes during the time span of our GPS data, such as the 2004 M_w 9.1 Sumatra-Andaman, the 2011 M_w 9.0 Tohoku-Oki, and all the $M_w \geq 5.9$ earthquakes in our study area. Details of coseismic and postseismic corrections are given in Table 2. After these corrections, we use a linear

Table 1
The Strategies of GPS Data Processing Using PANDA

Functions	Strategies
Supporting inputs	Use Earth rotation parameters, precise ephemeris in IGS08 reference frame and 30s satellite clock products from MIT, and differential code biases from CODE
Troposphere	Saastamoinen model (Saastamoinen, 1973) and GMF projection function (Boehm et al., 2006)
Ionosphere	Ionosphere-free linear combination (Zumberge et al., 1997)
Ocean tide correction	Online calculator (Bos and Scherneck; http://holt.oso.chalmers.se/loading) with the FES2004 model (Lyard et al., 2006)
Other corrections	Absolute antenna phase-center correction (Schmid et al., 2007) and phase wind-up correction (Wu et al., 1993)
Cutoff elevation angle	15°, use an elevation-dependent weighting strategy at low elevations (Gendt et al., 2003)

function to estimate velocities from position time series under a least squares criterion. The velocities are then transformed into the Eurasia-fixed frame according to the IGS08-Eurasia Euler vector given by Kreemer et al. (2014) ($wx = -0.0247$, $wy = -0.1418$, $wz = 0.2093$°/Myr). Thus, we obtain our core velocity field with 1556 CMONOC-I/II stations.

2.2. Velocity Field Combination

Kreemer et al. (2014) compiled a global GPS velocity field, which included 2263 stations from 32 studies in the India-Eurasia collision zone. Among these data, 127 continuous and 1116 campaign stations are also in our CMONOC-I/II solution. Considering that our observations span at least 2.5 years longer than those in Kreemer et al. (2014), we take use of our velocities directly for the common stations. Our updated velocities are more reliable, particularly for the 165 campaign stations that were observed only twice in Kreemer et al. (2014) taken from Liang et al. (2013). Subtle differences might exist for the reference frame, although Kreemer et al. (2014) used IGS08 as well. Using the 1078 common stations observed at least three epochs, we calculate an Euler vector ($wx = 0.0015$, $wy = 0.0049$, $wz = -0.0030$°/Myr) and then apply it to convert the 1020 uncommon stations observed from 1991 to 2013 in Kreemer et al. (2014) into our solution. Note that such conversion only results in changes of less than 0.7 mm/yr for the stations in Kreemer et al. (2014).

We estimate the uncertainties of the velocities using a least squares method. It is well known that the uncertainties may be underestimated particularly for the continuous stations if the flicker noise and random walk in the time series are unaccounted for (Kreemer et al., 2014; Langbein, 2012). To obtain consistent uncertainties with Kreemer et al. (2014), we reweight our core velocity field by multiplying the standard deviations with a scale factor between the average uncertainty in Kreemer et al. (2014) and ours. The factors are 2.4 and 3.4 for the east and north components, respectively. Figure 2 shows our resultant velocity field which contains 2576 stations in total.

2.3. Strain Rate Calculation

We model the strain rate fields using the method in Wang and Wright (2012). We divide the study area into a triangular mesh (Figure S1 in the supporting information) and assume that the velocity field within each

Table 2
The Strategies of Coseismic and Postseismic Corrections

Events	Strategies
2001 M_w 7.8 Kokoxili	(1) For CMONOC-I, we only use preseismic data of the sites within 400 km from the epicenter and apply a heaviside step function to correct coseismic deformation for the far-field sites (2) For CMONOC-II, we ignore postseismic deformation according to Ryder et al. (2011)
2004 M_w 9.1 Sumatra-Andaman	We use a heaviside step function to estimate coseismic offsets, and ignore postseismic deformation since CMONOC GPS stations are more than 2000 km away from the epicenter
2008 M_w 7.9 Wenchuan, 2011 M_w 9.0 Tohoku-Oki, and 2015 M_w 7.8 Nepal	We only use preseismic data of the affected stations and remove the affected continuous stations with less than 0.5-year preseismic measurements
Other $M_w \geq 5.9$ events	(1) For the near-field sites, we only use preseismic data and remove the continuous sites with less than 0.5-year preseismic observations (2) For the far-field sites, we use a heaviside step function to estimate coseismic deformation if observations are enough. Otherwise, we estimate velocities using either preseismic or postseismic data

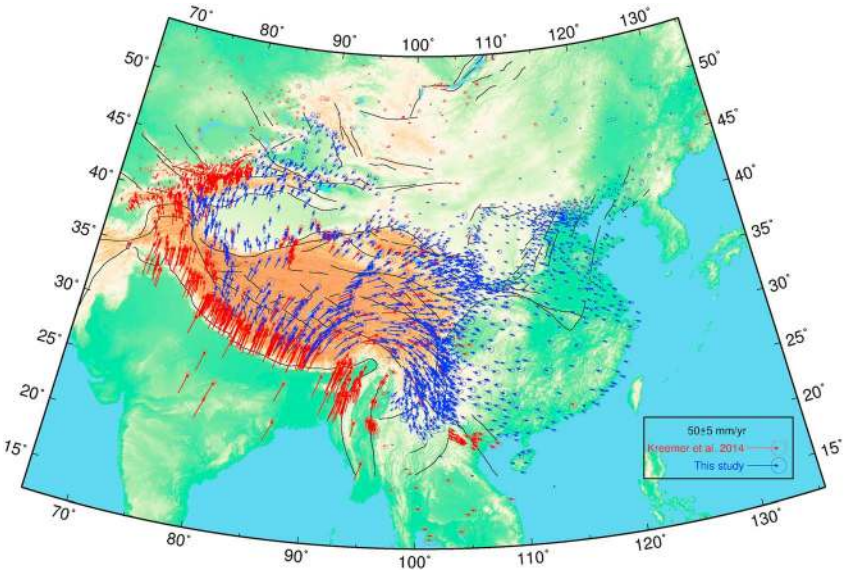

Figure 2. Interseismic GPS velocity field covering the India-Eurasia collision zone with respect to stable Eurasia. The blue arrows indicate the GPS velocities at CMONOC-I/II stations, and the red ones are those transformed from Kreemer et al. (2014). Error ellipses are 95% confidence interval.

triangle varies linearly with longitude and latitude. The velocities at the mesh vertices are regularized by Laplacian smoothing, with an optimal smoothing factor of 0.1 determined using an L-curve between solution roughness and weighted misfit (Figure S2). Here we use the cross-validation method to evaluate the quality of our velocity field model. We randomly discard 500 stations and use the rest to make a velocity field model. For the discarded stations, the differences between the predicted and the observed velocities are within 2 mm/yr at 95% level and over 70% of the residuals are smaller than 1 mm/yr (Figure 3), indicating that the results of our model are reliable. Then we use all the GPS stations to model the final velocity field. Based

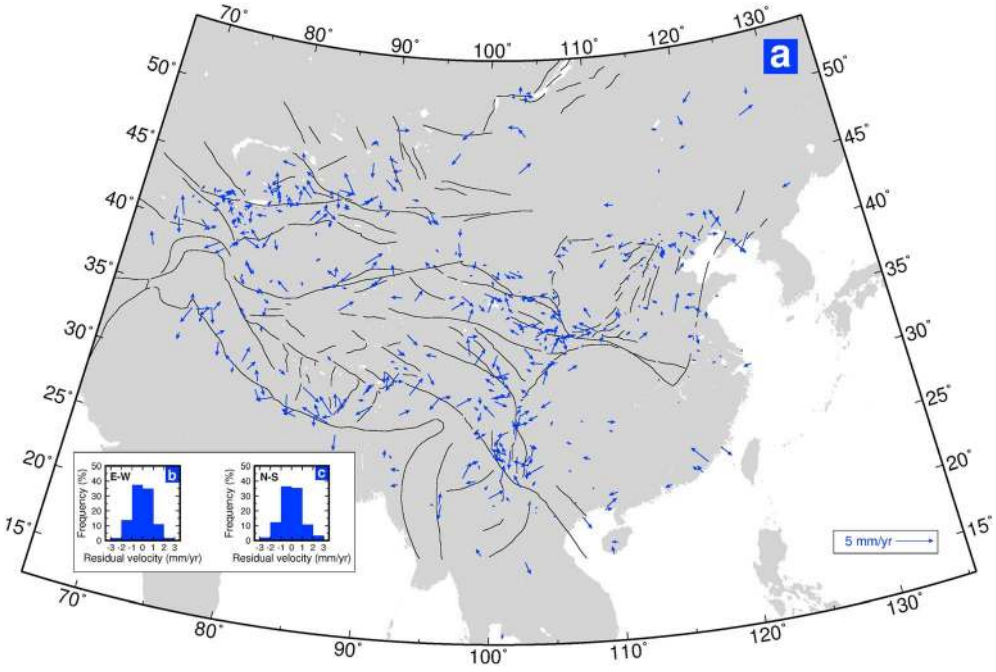

Figure 3. (a) The differences between the predicted and the observed velocities at 500 discarded stations. (b and c) Histograms for differences of the E-W and the N-S components, respectively.

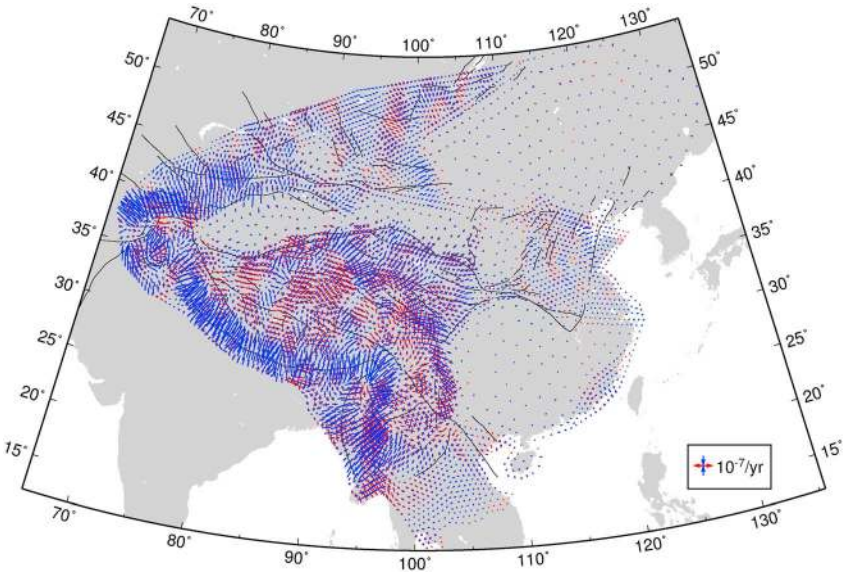

Figure 4. Principal strain rate field. Blue and red bars indicate the principal compressional and extensional strain rates at the vertices of the mesh shown in Figure S1, respectively.

on the predicted velocities at the mesh vertices, we calculate rotation and strain rates using spherical approximation equations (Savage et al., 2001). The resultant distributions of principal strain rate, second invariant of strain rate tensor, dilatational strain rate, and maximum shear strain rate are shown in Figures 4, 5a, 5b, and 5c, respectively.

3. Analysis

3.1. Geodetic Slip Rates of the Major Faults

Our new GPS velocity field gives us the opportunity to reevaluate geodetic estimates of slip rates for the major faults in the region. Rather than modeling the individual faults, we take a simpler approach and simply look at the differences in fault-normal/parallel velocities across each fault zone. The stations in the vicinity of locked structures (usually within ~50 km from the faults) will be influenced by elastic deformation around the fault (Duvall & Clark, 2010; Savage & Burford, 1973; Vernant, 2015), so in most cases we take the slip rate as the difference between the average velocities of the far-field stations (50–200 km away from the fault) on either side of the fault. The structure of the fault may be complex with several branches; here we assume that all deformation across a fault zone is concentrated on a single structure, which may lead to an overestimate of the slip rate on the primary structure if there is off-fault deformation or parallel structure.

The Himalayan frontal thrust is the dominant thrust belt in the India-Eurasia collision zone and accommodates a large fraction of the India-Eurasia convergence that is responsible for the recurrent great Himalayan earthquakes (Bilham et al., 1997). The current convergence rate is a key to understand the dynamics of mountain-building and the seismic cycle in the Himalaya. Many geodetic studies (e.g., Ader et al., 2012; Banerjee et al., 2008; Bettinelli et al., 2006; Bilham et al., 1997; Larson et al., 1999) have been conducted over decades, giving convergence rates of ~10–24 mm/yr along the Himalaya. However, discrepancies still exist for some segments due to the distribution of GPS sites in these studies. For instance, estimates for the shortening rate in the western Nepal Himalaya vary from ~13 mm/yr (e.g., Bettinelli et al., 2006) to ~21 mm/yr (e.g., Ader et al., 2012). Using more GPS data, we obtain an almost uniform shortening rate of ~15 mm/yr along four profiles HM1–HM4 normal to the Himalayan arc at ~77.5–93°E (Figures 6a–6d). The locations of our profiles are almost the same with Banerjee et al. (2008), who estimated a shortening rate of ~17 mm/yr. Note that the stations that we used for the slip rate calculation along the shallowly dipping Himalayan frontal thrust were different to those used for the other faults—we obtained the slip rate by comparing the velocities of sites immediately to the south of the fault with those 275–500 km north of the fault, consistent with the approach used by Banerjee et al. (2008).

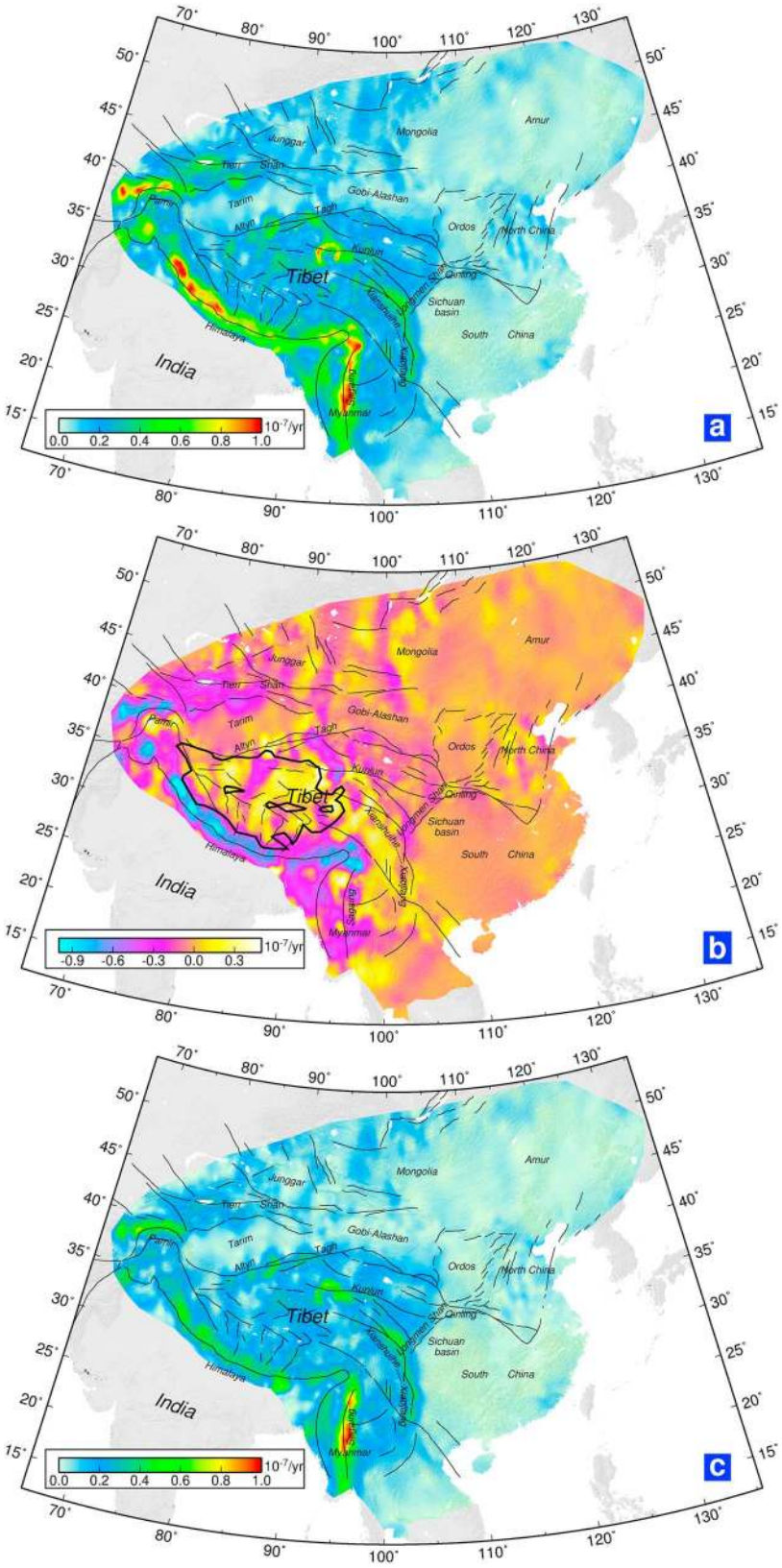

Figure 5. (a) Distribution of second invariant of strain rate tensor. (b) Dilatational strain rate field. Crustal extension is positive. Topography is Gaussian filtered with a 1° width, and the 4750 m contour is shown by a black line. (c) Maximum shear strain rate field.

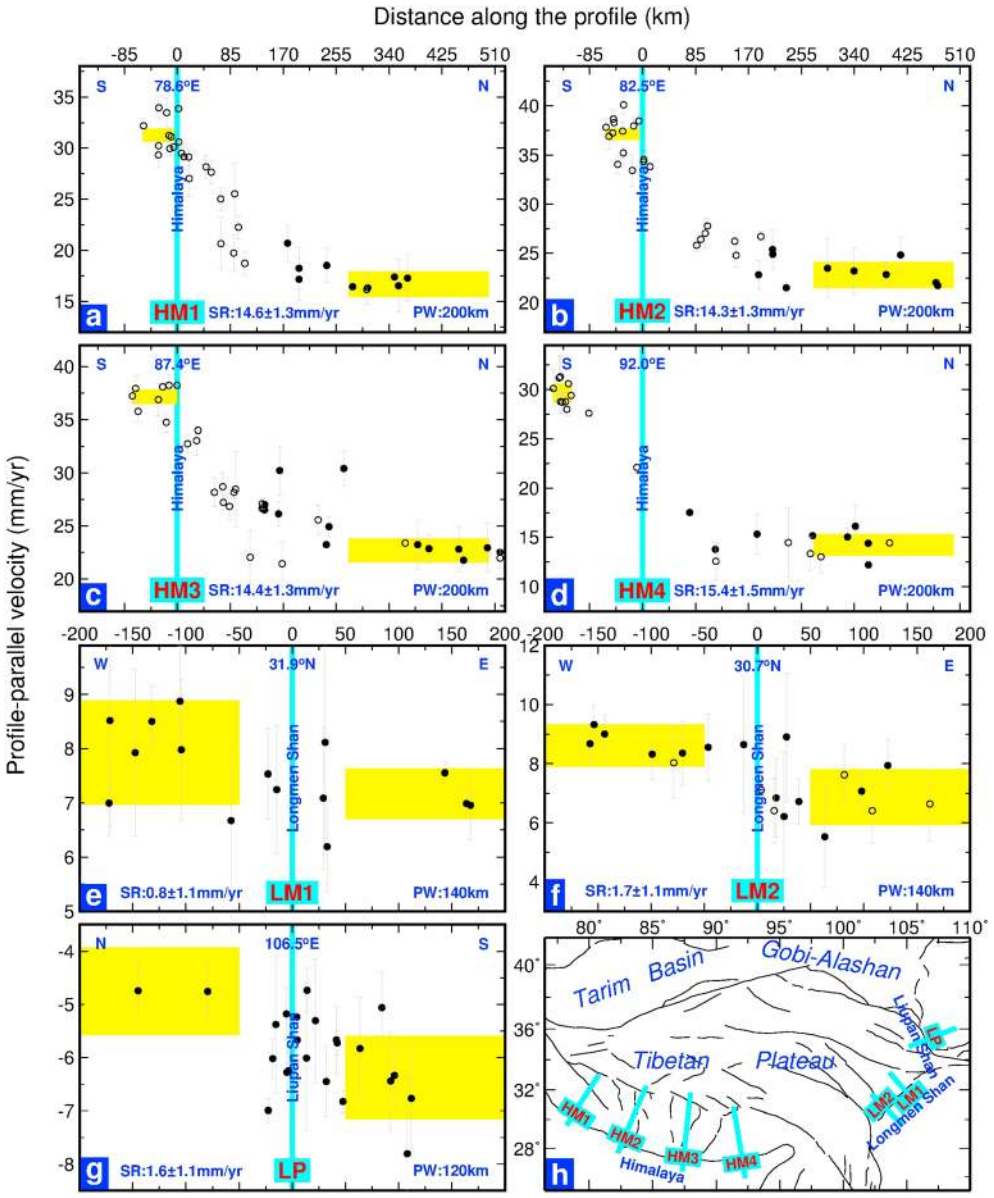

Figure 6. (a–g) GPS velocity profiles with 1 sigma error bar across the major thrust structures in Tibet. The solid symbols indicate the GPS velocities from the CMONOC-I/II stations while the open symbols for those from Kreemer et al. (2014), PW represents the width of the profile, the yellow bars denote the average rates of the stations used for slip rate calculation on either side of the fault with 95% confidence interval, and SR represents the slip rate also with 95% confidence interval (shortening and dextral rates are positive), all the same in the following. (h) The locations and labels of the profiles in Figures 6a–6g.

The Longmen Shan is the major thrust zone in eastern Tibet that has risen ~6000 m above the Sichuan basin (Burchfiel et al., 1995). It is the site of the 2008 Wenchuan and 2013 Lushan earthquakes. Previous geodetic studies presented shortening rates of ≤3 mm/yr across Longmen Shan (e.g., Chen et al., 2000; King et al., 1997; Shen et al., 2005; Zhang et al., 2004). Due to this low deformation rate also supported by geological investigations (e.g., Burchfiel et al., 1995; Densmore et al., 2007), it was widely considered that the seismic risk was low before the Wenchuan earthquake (Zhang, 2013a). Two profiles LM1 and LM2 through our velocity field (Figure 6h) give negligible dextral rates of ≤0.5 mm/yr (Figures S3a and S3b) and convergence rates of ~1–2 mm/yr (Figures 6e and 6f) across Longmen Shan, consistent with previous studies.

The Liupan Shan is an important thrust zone in the northeast corner of Tibet, bounding the plateau to the southwest and Ordos to the northeast (Zhang et al., 1991). The shortening rate is 1.6 ± 1.1 mm/yr (the error bar for this and subsequent slip rates denotes the 95% confidence interval) along the profile LP across Liupan Shan (Figure 6g), which is smaller than the geodetic estimate of 6 mm/yr in Zhang et al. (2004). In fact, the 6 mm/yr rate is the total shortening rate of Liupan Shan and an ~300-km-wide region west of it. We find an insignificant sinistral rate of 0.6 ± 1.3 mm/yr across Liupan Shan (Figure S3c).

The Altyn Tagh Fault extends for ~2000 km and marks the northern margin of the Tibetan Plateau. In its western segment, previous geodetic studies gave sinistral rates of 5–7 mm/yr (e.g., Shen et al., 2001; Wright et al., 2004). Using many more GPS sites than Shen et al. (2001), we obtain a lower sinistral rate of 1.4 ± 1.3 mm/yr from profile AT1 across the western segment (Figure 7a). In the central segment, two profiles AT2 and AT3 show sinistral rates of ~8–9 mm/yr (Figures 7b and 7c). We find that our results are consistent with a uniform rate of ~8–11 mm/yr from previous geodetic studies along the central Altyn Tagh Fault at ~84–94°E (e.g., Bendick et al., 2000; Elliott et al., 2008; He et al., 2013; Jolivet et al., 2008; Shen et al., 2001; Zhang et al., 2007). Further east, we obtain 4.5 ± 0.9 mm/yr sinistral rate from the profile AT4 near ~95°E (Figure 7d), comparable to the geodetic estimate in Zhang et al. (2007) near 96°E. We find shortening rates of $\leq$3 mm/yr along the Altyn Tagh Fault (Figures S4a–S4d).

The ~1000-km-long Haiyuan Fault accommodates the relative motion between the Gobi-Alashan platform and northeastern Tibet. It is the site of two M_w~8 earthquakes in the last century—the 1920 Haiyuan and the 1927 Gulang earthquakes. Except for the estimate of ~10 mm/yr from Daout et al. (2016), previous geodetic studies showed strike-slip rates of ~4–6 mm/yr along the main Haiyuan Fault (e.g., Cavalié et al., 2008; Duvall & Clark, 2010; Jolivet et al., 2012; Zheng et al., 2013). Here two profiles HY1 and HY2 across the main Haiyuan Fault give a sinistral rate of ~4–5 mm/yr (Figures 7e and 7f) and a shortening rate of ~2–3 mm/yr (Figures S4e and S4f), inconsistent with a present-day strike-slip rate of 10 mm/yr.

The ~1600-km-long Kunlun Fault contributes to the eastward movement of the Songpan "block" with respect to northern Tibet. Our three profiles KL1–KL3 across the Kunlun Fault show sinistral rates of 12.8 ± 1.9, 6.1 ± 0.9, and 0.7 ± 2.1 mm/yr near ~94°E, ~101°E, and ~103°E, respectively (Figures 7g–7i), while the deformation rates normal to the strike along the fault are insignificant ($<$2 mm/yr) (Figures S4g–S4i). Our strike-slip rates are consistent with previous geodetic studies (e.g., Chen et al., 2000; Garthwaite et al., 2013; Wang et al., 2001; Zhang et al., 2004).

The Xianshuihe-Xiaojiang fault system runs for ~1200 km from northwestern Sichuan to southern Yunnan. It is composed of a series of active faults including the Xianshuihe, Anninghe, Zemuhe, and Xiaojiang segments from north to south. It is the major structure facilitating the clockwise rotation of southeastern Tibet relative to South China around the Eastern Himalayan Syntaxis. Previous geodetic studies showed sinistral rates of ~7–12 mm/yr along this fault system (e.g., Chen et al., 2000; King et al., 1997; Rui & Stamps, 2016; Shen et al., 2005; Wang et al., 2009). Here three profiles XS, AN, and ZM give ~9 mm/yr sinistral rate across the Xianshuihe-Zemuhe segment (Figures 7j–7l), while the profile XJ gives ~7 mm/yr sinistral rate across the Xiaojiang Fault (Figure 7m). In addition, we find that most portions of this fault system have a normal-slip motion of ~1–3 mm/yr while the Anninghe segment has a reverse-slip motion of ~5 mm/yr (Figures S4j–S4m). Note that the slip rates for the Anninghe and Zemuhe Faults include the effect of the adjacent Daliangshan block (Rui & Stamps, 2016).

The Karakoram Fault extends for ~1000 km from north of the Himalaya to Pamir, associated with the northward advancement of the Western Himalayan Syntaxis into Eurasia. Except for the estimate of 11 mm/yr from Banerjee and Bürgmann (2002), previous geodetic studies showed low strike-slip rates of ~0–6 mm/yr along the Karakoram Fault (e.g., Jade et al., 2004; Kundu et al., 2014; Wang & Wright, 2012; Wright et al., 2004). Here three profiles KR1–KR3 across the Karakoram Fault give dextral rates of 6.0 ± 1.5, 3.8 ± 2.5, and 3.2 ± 2.3 mm/yr near ~77°E, ~79°E, and ~81°E, respectively (Figures 7n–7p), confirming a low slip rate at present. In addition, we estimate shortening rates of 5 ± 1.5 and 0.5 ± 2.5 mm/yr near ~77°E and ~81°E, respectively, and an extensional rate of 3.3 ± 2.5 mm/yr near ~79°E (Figures S4n–S4p).

The $>$1000-km-long Red River fault is the major site of the sinistral motion between South China and Indochina during the southeastward extrusion of Indochina driven by the India-Eurasia collision. It is thought to have reversed its sense of slip from sinistral to dextral as the continuous collision led to the eastward extrusion of South China (Tapponnier et al., 1982). Along the China segment of the Red River

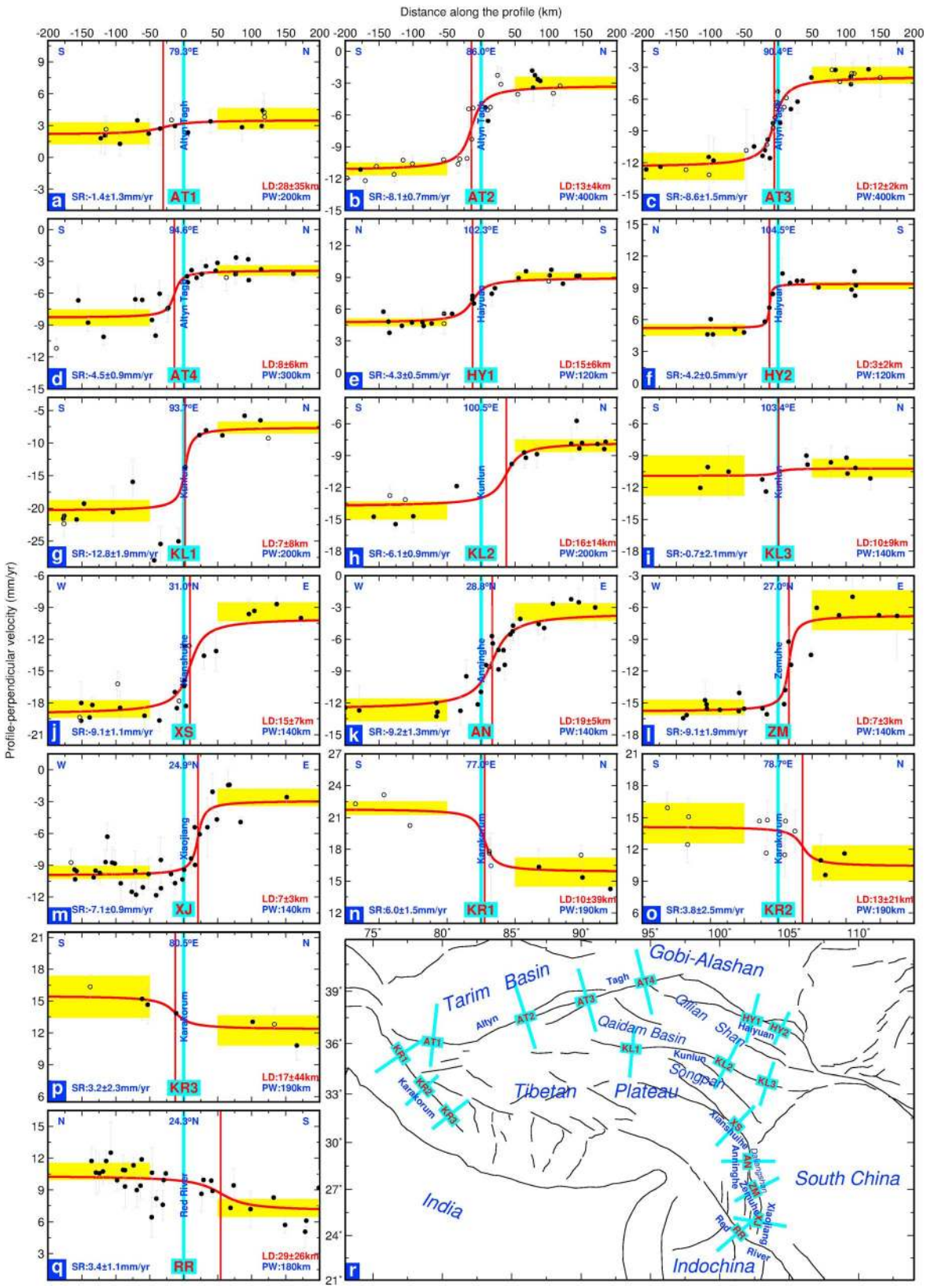

Figure 7. GPS velocity profiles with 1-sigma error bar across the major strike-slip faults in Tibet. The locations and labels of the profiles in Figures 7a–7q are shown in Figure 7 r. LD represents the locking depth with 1-sigma error bar. Note that a station along the profile KR1 shown as a blue circle from Kreemer et al. (2014) has a high observed error; if we include it in the locking depth calculation, we will get a very shallow locking depth that we doubt, so here we reject it in the calculation.

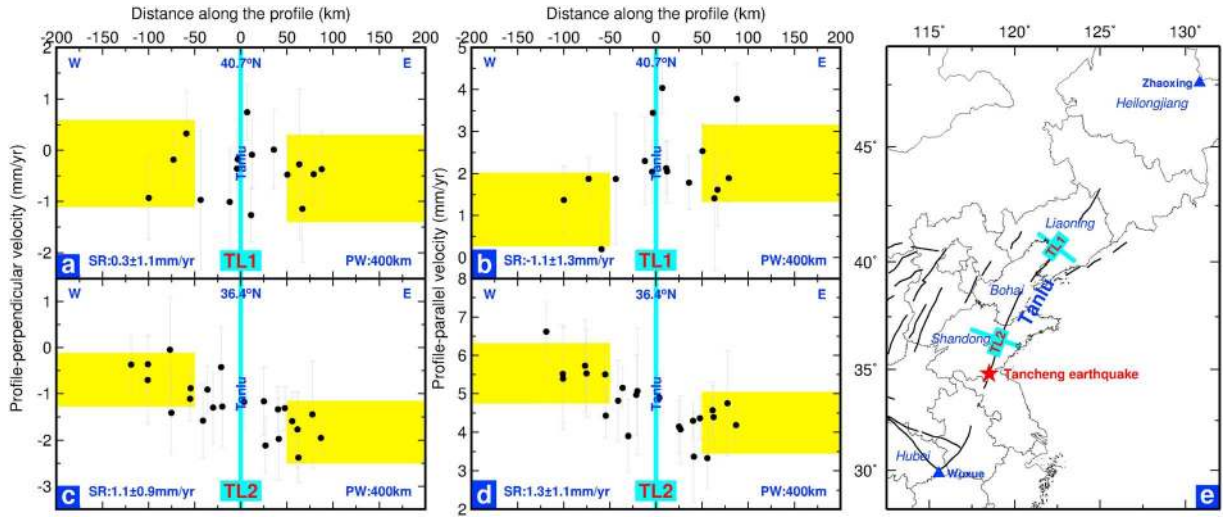

Figure 8. GPS velocity profiles with 1-sigma error bar across the Tanlu Fault. The locations and labels of the profiles are shown in Figure 8e. The black fine lines in Figure 8e show the provincial boundaries in China, and the red star indicates the probable epicenter of the 1668 Tancheng earthquake.

fault, previous geodetic studies showed dextral rates of ~1–2 mm/yr (e.g., Hao et al., 2014; Shen et al., 2005). Using more GPS stations than were available in previous studies, we obtain a dextral rate of 3.4 ± 1.1 mm/yr (Figure 7q) and a negligible extensional rate of 0.4 ± 1.1 mm/yr (Figure S4q) across the China segment along profile RR.

Outside Tibet, an important fault is the Tanlu Fault in East China; it is about 2400 km long, extending from Wuxue in Hubei Province to Zhaoxing in Heilongjiang Province, and may be even up to ~3600 km long if we consider its extent into Russia (Huang et al., 1996). The Liaoning-Bohai-Shandong segment is historically the most dangerous part, and is the probable location of the 1668 *M* 8.5 Tancheng earthquake—the largest known event in East China (Huang et al., 1996). However, geodetic slip rates along the Liaoning-Bohai-Shandong segment have been poorly constrained. With limited GPS sites, Shen et al. (2000) suggested an approximate range of $\leq$3 mm/yr for the Shandong segment. Here the profile TL1 gives 0.3 ± 1.1 mm/yr dextral rate across the Liaoning-Bohai segment (Figure 8a), while the profile TL2 gives 1.1 ± 0.9 mm/yr dextral rate across the Shandong segment (Figure 8c). In addition, we find dip-slip partitioning as suggested by Deng et al. (2003): the Liaoning-Bohai segment has a normal-slip motion of 1.1 ± 1.3 mm/yr (Figure 8b), whereas the Shandong segment has a reverse-slip motion of 1.3 ± 1.1 mm/yr (Figure 8d).

One way of assessing the degree to which strain is focused on a single structure is to estimate the locking depth using simple dislocation models (e.g., Savage & Burford, 1973). To do this we use a simple inversion on the profiles across the major Tibetan strike-slip faults as shown in Figure 7, fixing slip rates to those we estimate above to calculate locking depths. We find that for most of the faults, deformation is consistent with being caused by elastic strain accumulation on the dominant structure within the profile, with our locking depth estimates within the range of 13 ± 6 km, found by Wright et al. (2013) to be typical for the region. There are three exceptions—profiles AT1, HY2, and RR. Although they are very poorly determined, the deep best-fit locking depths of ~29 km along profiles AT1 and RR suggest that other adjacent faults may be involved in these two locations (Allen et al., 1984; Yin et al., 2002); the very shallow locking depth of ~3 km along profile HY2 is consistent with previous interpretations of shallow creep in this region (e.g., Jolivet et al., 2012, 2015).

In summary, our updated geodetic slip rates provide the most reliable estimates of rates of present-day geodetic strain accumulation for the major faults in the India-Eurasia collision zone. In most cases our rates are consistent with previous geodetic (both GPS and InSAR) estimates. However, we benefit from the increases in the number of stations and the durations of station occupations.

3.2. Key Features of the Velocity Field

Here we describe the key features of our new velocity field for the India-Eurasia collision zone. We focus on the irreducible features that have emerged as GPS observation density and accuracy have improved. These fundamental features provide a test that models of continental deformation must pass. They are the following: (i)

there are several large undeforming regions within the collision zone, (ii) some major faults are visible in the velocity field due to strain concentrations, (iii) there are regions of diffuse deformation, and (iv) the high-elevation regions of Tibet are dilating. Below, we describe each of these key features in more details.

3.2.1. Undeforming Regions

It is immediately apparent on examining all components of the velocity field (Figures 4 and 5) that deformation is not uniformly and smoothly distributed within the collision zone. On the largest scale, the deformation in the India-Eurasia collision zone almost exclusively occurs within the Eurasian plate, while the Indian plate does not deform significantly. Within our velocity field we see clear other examples of non-deforming regions embedded within otherwise deforming regions. These are characterized by having low strain rates in their interiors and relatively high strain rates around their boundaries.

The largest of these non-deforming regions stretches from ~75 to 105°E, including the Tarim basin in the west and the Gobi-Alashan platform in the east (Figure 5). This region is an ~300–400 km wide band of low strain along the entire northern boundary of the Tibetan Plateau and bounds the Tien Shan mountains to the north.

The two other large undeforming regions are the Sichuan and Ordos basins (Figure 5). The Sichuan basin marks the eastern limit of the Tibetan Plateau and is bound to the NW by the Longmen Shan. The 2008 M_w 7.9 Wenchuan earthquake (Shen et al., 2009) resulted from thrusting along this boundary. The Xianshuihe-Xiaojiang fault system bounds the western edge of this block, and the northern limit is marked by the Qinling fault system. Our velocity field suggests that the Sichuan basin moves coherently with South China. The Ordos basin is an isolated region of low strain at the NE limit of the Tibetan Plateau, surrounded by extensional rifts (Zhang et al., 1998).

3.2.2. Strain Concentrations Around Some Major Faults

A striking feature of our velocity field, and those produced by others (e.g., Kreemer et al., 2014), is the concentration of strain around some of the major faults in the region (Figure 5a). The prominent among these are the Himalayan Frontal Thrust, the boundaries of the Tien Shan, and the strike-slip Altyn Tagh, Kunlun, Xianshuihe-Xiaojiang, and Sagaing fault zones. In these regions, strain rates typically exceed 40 nanostrain/yr (Figure 5a), compared to an average rate of ~18 nanostrain/yr for most of the Tibetan Plateau away from these zones (Figure S5). As well as in map view, the strain concentrations can clearly be seen in the original data in fault-normal velocity profiles (Figures 6a–6d, 7a–7d, and 7g–7m).

The Himalayan Frontal Thrust and the Sagaing fault zone are plate-bounding faults, marking the northern and eastern limits, respectively, of the Indian plate. These faults form part of a complete network of faults that surround the Indian plate, allowing it to move as a discrete plate with minimal internal deformation. By contrast, the Altyn Tagh, Kunlun, and Xianshuihe-Xiaojiang fault zones are embedded within the deforming Eurasian plate. The faults, and their strain signatures, are discrete structures; their strain rates change along their length (section 4.1) and they have clear ends (Figure 5a). They do not surround isolated discrete blocks.

3.2.3. Regions of Diffuse Deformation

While some of the major faults show strain concentrations, another fundamental feature of the velocity field for the collision zone is that there are large regions of diffuse strain. The most prominent of these is the Tibetan Plateau, which is straining at an average rate of ~18 nanostrain/yr in the interior of the plateau (outlined in Figure S5; away from the main faults—the Altyn Tagh, Kunlun, and Xianshuihe-Xiaojiang Faults and the Himalayan Frontal Thrust). This diffuse deformation is clearly visible in the individual components of the strain tensor (Figures 4, 5b, and 5c) as well as in the second invariant map (Figure 5a).

In previous velocity fields, it has been reasonable to suggest that a cause of apparent diffuse strain is poor station density. Our improved station density and measurement accuracy give us increased confidence that we really do see diffuse deformation for large parts of the region. This is clearly visible in individual profiles through the original data spanning large regions of the plateau (Figure 9). For example, NNE-SSW profiles TP1–TP3 spanning the plateau show convergence of ~10 mm/yr that is distributed uniformly across a distance of ~700 km within the plateau (away from the Himalaya and the Altyn Tagh Fault; Figure 9a). Similarly, profile TP4 shows extension of ~15 mm/yr across southern Tibet that appears to be uniformly distributed on a length scale of ~1500 km (Figure 9b).

3.2.4. Dilation of the High-Elevation Regions of Tibet

The highest elevations of the Tibetan Plateau have long been known to undergo extension due to normal faulting on the basis of earthquake focal mechanisms, interpretations of satellite imagery, and field

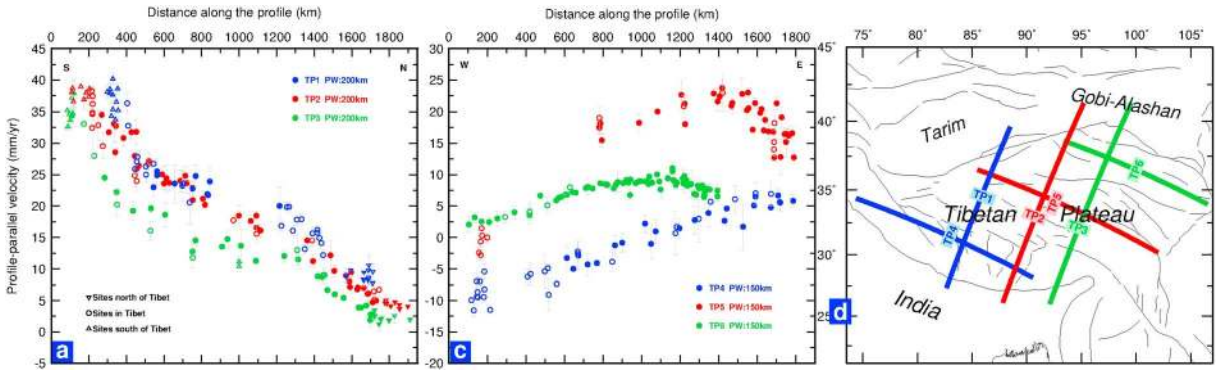

Figure 9. GPS velocity profiles with 1-sigma error bar across the Tibetan Plateau (TP1–TP6). The locations and labels of the profiles in Figures 9a and 9b are shown with the same colors in Figure 9c.

investigations (e.g., Armijo et al., 1986; Molnar & Chen, 1983; Molnar & Tapponnier, 1978; Ni & York, 1978). However, it has been unclear whether extension outpaces convergence, leading to horizontal dilation and crustal thinning (assuming conservation of volume) for the entire plateau (e.g., Elliott et al., 2010; Molnar et al., 1993), or if thinning is focused primarily in the south of Tibet (e.g., Armijo et al., 1986; Copley et al., 2011).

Recently, Ge et al. (2015) used an earlier GPS velocity field to map the rates of dilation in the Tibetan Plateau. They found that the rates of horizontal dilation for the northern and southern plateau are similar at ~9 and ~7 nanostrain/yr, respectively. We use our updated velocity field to reestimate the dilation field for the India-Eurasia collision zone (Figure 5b). Like Ge et al. (2015), we find that dilation is occurring at a similar rate for northern and southern Tibet (see Figure S6 for their outlines), with average rates of ~7 and ~5 nanostrain/yr, respectively. Like Elliott et al. (2010), we find that dilation within the plateau is strongest at elevations higher than ~4750 m, suggesting that gravitational potential energy is controlling the process.

Our dilation field in Figure 5b also shows several bands of apparent convergence that are parallel to the convergence direction. While we hesitate to interpret these shorter (~100 km) wavelength features in what remains a noisy velocity field, we note that anomalies on similar length scales have been observed in finite frequency body wave tomography models (Liang et al., 2016) and have been interpreted in terms of short-wavelength convective instabilities (Houseman & England, 2017).

4. Discussion

4.1. Along-Strike Change in the Slip Rate

Many studies have presented a decrease in the sinistral rate eastward along the Altyn Tagh Fault (e.g., Chen et al., 2000; Mériaux et al., 2005; Xu et al., 2005; Zhang et al., 2007). Regardless of the rate discrepancies with some studies, our profile results also show an eastward decrease in slip rate, varying from ~8–9 mm/yr along the central segment (Figures 7b and 7c) to ~4–5 mm/yr near 95°E in the eastern segment (Figure 7d). This feature requires deformation of the region surrounding the eastern tip of the fault. As Tarim on one side is rigid, internal shortening of the Qilian Shan thrust belt on the other side of the fault tip must be responsible for the decreasing slip rate (Zhang et al., 2007).

Similarly, our results (Figures 7h and 7i) together with Kirby et al. (2007), Harkins and Kirby (2008), Lin and Guo (2008), and Harkins et al. (2010) show that the eastern segment of the Kunlun Fault also has an eastward decreasing sinistral rate. This decrease may begin near the eastern end of the Qaidam basin from ~12 mm/yr (Duvall & Clark, 2010). Loveless and Meade (2011) indicated that the Elashan and Riyueshan Faults intersected with the eastern Kunlun Fault each transfer slip of ~5 mm/yr away and result in the decrease of slip rate. However, these two faults were shown to slip with a low rate of ~1 mm/yr by Yuan et al. (2011). Duvall and Clark (2010) indicated that the decreasing slip is transferred northward, and accommodated by internal deformation of a region north of the fault with a north-south width of ~500 km. However, they ignored significant deformation in the region south of the eastern Kunlun Fault, which was shown by the red triangles in their Figure 3. Our preferred interpretation was provided by Kirby and Harkins (2013), that crustal thickening across the Anyemaqen Shan and clockwise rotation of the eastern Kunlun Fault, driven by the NE-striking dextral shear across it, now associated with the Longriba fault zone

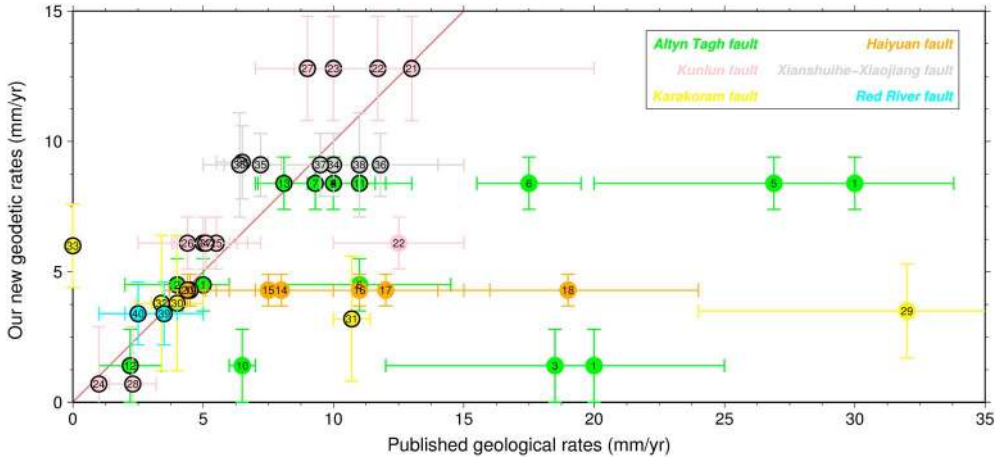

Figure 10. Geodetic slip rates with 95% confidence interval derived in this study versus published geological estimates for the major strike-slip faults within Tibet. The numbers represent (1) Peltzer et al. (1989), (2) Meyer et al. (1996), (3) Ryerson et al. (1999), (4) Washburn et al. (2001), (5) Mériaux et al. (2004), (6) Xu et al. (2005), (7) Cowgill (2007), (8) Zhang et al. (2007), (9) Cowgill et al. (2009), (10) Li, Van der Woerd, et al. (2012), (11) Chen et al. (2013), (12) Li et al. (2016), (13) Gold et al. (2017), (14) Zhang et al. (1988), (15) Burchfiel et al. (1991), (16) Gaudemer et al. (1995), (17) Lasserre et al. (1999), (18) Lasserre et al. (2002), (19) Li et al. (2009), (20) Zheng et al. (2013), (21) Kidd and Molnar (1988), (22) Van Der Woerd et al. (2002), (23) Li et al. (2005), (24) Kirby et al. (2007), (25) Harkins and Kirby (2008), (26) Harkins et al. (2010), (27) Gold and Cowgill (2011), (28) Ren et al. (2013), (29) Liu (1993), (30) Brown et al. (2002), (31) Chevalier et al. (2005), (32) Chevalier et al. (2015), (33) Robinson et al. (2015), (34) Allen et al. (1991), (35) Wen et al. (1996), (36) Xu et al. (2003), (37) Zhang (2013b), (38) Ren et al. (2010), (39) Allen et al. (1984), and (40) Weldon et al. (1994). We add black bounds to the circles that denote the well-constrained and most recent geological estimates.

(Xu et al., 2008), accommodate the eastward decrease in slip rate. We note that variations in the slip rate along long faults (e.g., the Altyn Tagh and Kunlun Faults) may also be a useful test for models of along-strike fault propagation (Perrin et al., 2016; Perrin Manighetti, & Gaudemer, 2016).

Along the Karakoram Fault, our profiles show decreasing dextral rates from northwest to southeast (Figures 7n–7p), which have not been found in Wang and Wright (2012) using InSAR and fewer GPS data. Kundu et al. (2014) showed similar result to ours. They suggested that it was because the India-Eurasia convergence direction becomes more oblique to the Himalaya toward the west, resulting in that more convergence is accommodated by the dextral slip of the Karakorum Fault. The propagation scenario of the Karakoram Fault is controversial (Murphy et al., 2000; Robinson, 2009; Valli et al., 2008; Wang et al., 2011). Some studies suggested that the fault propagates southward (e.g., Murphy et al., 2000), and this was consistent with the southeastward decrease of slip rates. However, GPS stations around the Karakoram Fault are still sparse. With the improvements of InSAR and GPS data, the spatial variation of the slip rates along the fault can be better constrained in the future.

4.2. A Comparison Between Geological and Geodetic Estimates of Slip Rates

Geodetic estimates of slip rates for the major strike-slip faults globally have been shown to be in reasonable agreement with estimates from geological observations (e.g., Meade et al., 2013; Thatcher, 2009). However, for some of the major strike-slip faults within the India-Eurasia collision zone, potential discrepancies have been much discussed (e.g., Chevalier et al., 2005; Cowgill, 2007; Cowgill et al., 2009; Mériaux et al., 2004). Here we compare our new geodetic slip rates against available geological estimates and critically assess any apparent discrepancies. Note that the geological rates we consider are all for the Quaternary to present or a shorter time span (e.g., Holocene). To compare these rates to geological rates, we of course assume that all the deformation we currently observed is elastic and is eventually released as slip in earthquakes, and that the present-day geodetic deformation rates, measured on a decadal timescale, are representative of the long-term geological rates, usually measured on timescales of thousands of years.

We focus on the six major strike-slip faults in Tibet—the Altyn Tagh, Haiyuan, Kunlun, Karakoram, Xianshuihe-Xiaojiang, and Red River Faults. A simple plot of our slip rate estimates for each of these faults against the available geological estimates in Figure 10 shows that our geodetic rates agree in general with the lower end of the range of geological estimates, which are often very scattered. Below we assess each fault in

turn, beginning with the Altyn Tagh Fault, and argue that the lower estimates of geological rates are in general more robust than the higher estimates.

For the east-central Altyn Tagh Fault, some early geological investigations found slip rates of ~20–30 mm/yr that were about 3 times higher than the geodetic estimates, and suggested that the disparate geological and geodetic rates may reflect time-variable fault behavior (e.g., Mériaux et al., 2004, 2005). But subsequent geological studies, such as Cowgill (2007) and Zhang et al. (2007), indicated that earlier studies may have suffered from systematic biases in the geomorphic reconstructions. Specifically the choice of whether to use the upper or lower terrace age as the reference date for the terrace riser has been controversial; using upper terrace ages to reinterpret published data for high rates, Cowgill (2007) and Zhang et al. (2007) obtained estimates of ~9–10 mm/yr that are consistent with our geodetic rate of ~8–9 mm/yr. Most recently, a geological analysis using a Monte Carlo method by Gold et al. (2017) also gave a rate of ~8 mm/yr for the past ~17 kyr. In the western segment of the Altyn Tagh Fault, published geological estimates have also decreased from initially high estimates of ~20 mm/yr (Peltzer et al., 1989; Ryerson et al., 1999), to subsequent more modest rate of ~7 mm/yr by Li, Van der Woerd, et al. (2012), finally to recent low rate of 1–3.5 mm/yr also by Li et al. (2016). This lower rate is consistent with our updated geodetic rate of 1.4 ± 1.3 mm/yr for the western Altyn Tagh Fault.

For the Haiyuan Fault, estimates of slip rates in early geological studies were also higher than geodetic results. Zhang et al. (1988) gave a slip rate of ~8 mm/yr, but their radiocarbon sample taking from the face of the terrace riser may suffer subsequent pollution by younger material sliding down the face, resulting in a younger age than the truth for the offset, and their offset measurement has been difficult to reproduce using modern methods (e.g., Li et al., 2009). Gaudemer et al. (1995) and Lasserre et al. (1999, 2002) gave ~10–20 mm/yr rates, all using lower terrace age to date the initiation of riser offset. However, no study has determined that whether upper or lower terrace age can approximately date the initiation of riser offset in the Haiyuan Fault; thus, the ages of both upper and lower terraces should be used for the lower and upper bounds of the actual rate, respectively. Zheng et al. (2013) reanalyzed the sites investigated by Lasserre et al. (1999, 2002) and found that both the sample positions and the measured offsets were disputable. Overcoming the shortcomings in the early geological studies, slip rates of ~4–5 mm/yr, consistent with our geodetic result of 4.3 ± 0.5 mm/yr, are given by recent geological studies (e.g., Li et al., 2009; Zheng et al., 2013).

For the Kunlun Fault, Van Der Woerd et al. (2002) gave a much higher slip rate (12.5 mm/yr) than our geodetic estimate of 6.1 ± 0.9 mm/yr near 101°E. They indicated that the upper bound of the age for their measured offset was younger than the Last Glacial Maximum (LGM). But as mentioned by some studies elsewhere (e.g., Brown et al., 2002; Hetzel et al., 2002), the actual age may be significantly older than the LGM. Also, the lower bound of the age may be too young as questioned by Harkins et al. (2010). Except for this estimate, other geological slip rates (~10–13 mm/yr for the west-central segment (e.g., Gold & Cowgill, 2011; Kidd & Molnar, 1988; Li et al., 2005; Van Der Woerd et al., 2002), ~5–6 mm/yr near 101°E (e.g., Gold & Cowgill, 2011; Harkins et al., 2010; Harkins & Kirby, 2008; Kirby et al., 2007), ~1–2 mm/yr near 103°E (e.g., Kirby et al., 2007; Ren et al., 2013) are consistent with our geodetic estimates given in section 3.1.

For the Karakoram Fault, Liu (1993) presented a very high geological rate of 32 mm/yr with an assumed age of 10 kyr, which was too young as suggested by Brown et al. (2002). Subsequently, the published geological slip rates are usually in the range of 0 to 11 mm/yr. Variable estimates in this range appear to be reasonable according to their related interpretations (e.g., Brown et al., 2002; Chevalier et al., 2005, 2015; Robinson et al., 2015), and it is likely that this scatter represents a realistic estimate of the uncertainty in the geological slip rates. It is therefore difficult to assess whether there is any discrepancy between geological and geodetic slip rates for the Karakoram Fault at present, and more field investigations at more sites along the fault are needed to reduce the uncertainty in the geological rates.

For the Xianshuihe-Xiaojiang fault system, previous geological slip rates ranged from ~5 to ~15 mm/yr (e.g., Allen et al., 1991; Ren et al., 2010; Wen et al., 1996; Xu et al., 2003; Zhang, 2013b), consistent with our geodetic estimates of ~7–9 mm/yr given the uncertainties. For the Red River fault, the Quaternary slip rate of ~2–5 mm/yr by Allen et al. (1984) agrees with our geodetic result. For a shorter term, a Holocene rate of ~1–4 mm/yr by Weldon et al. (1994) is also consistent with our geodetic rate.

For the slip rates of the major Tibetan strike-slip faults at least one geological estimate (usually the most recent/robust; circled with a black bound in Figure 10) is consistent with the geodetic rate, although of course the agreement between these rates and geodetic rates does not necessarily mean that they also do not suffer

from systematic or methodological errors that have been underestimated by the authors. Therefore, we do not see any evidence for a verifiable discrepancy between geodetic and geological rates in this region. If true, then this result implies that geodetic strain builds up at a reasonable constant rate through time around the major structures and that the geodetic strain rates can be a useful input data set for seismic hazard assessment (e.g., Bird et al., 2015; Bird & Kreemer, 2015; Bird et al., 2010).

4.3. Block Versus Continuum Models, Implications for Dynamics of the India-Eurasia Collision

The key irreducible features of deformation within the India-Eurasia collision zone (section 3.2) provide a simple checklist against which to evaluate contrasting models of continental tectonics. As described in section 1.1, the debate has often been framed (Thatcher, 1995, 2009) as a contrast between "microplate" or "block" tectonics and "continuum" models. Geodetic data are now of sufficient quality for us to assess these models critically against the key observations.

First, successful models must be capable of producing large regions low strain rates, ranging in scale from large continental regions such as the Indian continental lithosphere to smaller regions such as the Sichuan basin. Block models of course are by design capable of producing large low-strain regions—the interiors of blocks are not allowed to deform. Continuum models can produce regions of low strain in two ways. The first of these is to give regions different material properties, for example, defining them as stronger inclusions within a generally weaker material (e.g., Neil & Houseman, 1997). Second, there can be regions where there are no forces acting to cause deformation—a region may not be strong but nevertheless will only deform if it is subjected to appropriate forces. This has been proposed as a mechanism to explain low-strain regions in the central Iranian and Turkish-Iranian plateaux (Walters et al., 2017). The presence of low-strain regions is therefore not a useful feature for discriminating between block and continuum models.

The presence of high-strain zones at some major faults is the second key characteristic of the velocity field. For block models that account for the elastic strain around their boundaries (e.g., McCaffrey, 2002), the presence of high-strain zones in observation is on the face of it strong supporting evidence for block models. However, a prediction of the microplate/block model would be that isolated blocks are completely surrounded by fault zones. While this is true on the largest scale for the Indian plate, it does not appear to be the case for the faults embedded within the deforming Eurasian continent. These faults have discrete ends. Furthermore, any variations in slip rate along block bounding faults should be consistent with the location of Euler rotation poles and the geometry of the faults. We would not expect variations in the strike-slip rate therefore for faults such as the Kunlun and Altyn Tagh Faults (section 4.1). So although the presence of strain concentrations appears to be consistent with block models, their distribution in space is inconsistent.

Thin viscous sheet continuum models are not designed to predict deformation at the scale of individual fault zones, and it is therefore not surprising that they also do not predict strain concentrations without special interventions. Nevertheless, Dayem et al. (2009) showed that a strong contrast in material strength can result in the concentration of strain in the weaker material. This mechanism can explain the strain concentration along the Altyn Tagh Fault, which lies on the Tibetan (weak) side of the Tarim basin, but does not provide an explanation for strain concentrations along faults embedded within Tibet, such as the Kunlun Fault. If these strain concentrations are long-term features, the presence of weaker material along the fault zone is required to produce them (e.g., Lechmann et al., 2011). Such weakening could be the natural result of strain localization mechanisms such as grain size reduction and shear heating (e.g., De Bresser et al., 2001; Kirby, 1985; Thatcher & England, 1998). Alternatively, strain concentrations around major faults may simply be transient effects due to the earthquake cycle—they arise naturally if the relaxation time of the viscoelastic lower crust is equal to or longer than the inter-event time (e.g., Elliott et al., 2016; Savage, 2000; Takeuchi & Fialko, 2012; Yamasaki et al., 2014).

The third key characteristic of the observed strain field is the presence of large regions with relatively homogeneous strain distributions. Such strain fields are features produced naturally by continuum models such as the thin viscous sheet model. Large regions of distributed strain are harder to produce with block models without either allowing the blocks to deform internally (e.g., Chen et al., 2004; Loveless & Meade, 2011) or increasing the number of blocks such that all points are influenced by elastic strain from the block boundaries (e.g., Floyd et al., 2010; Hammond et al., 2011).

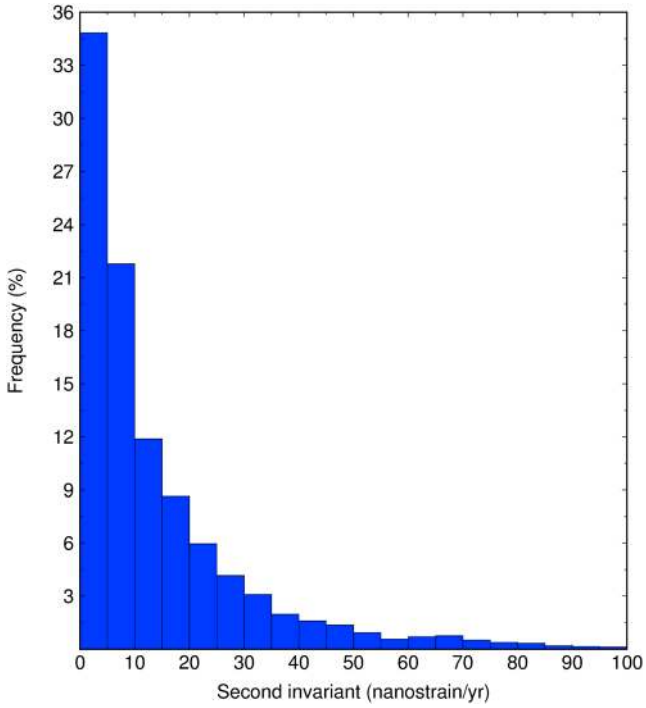

Figure 11. Histogram showing the distribution by area of the magnitude of the second invariant of strain rate tensor for our study region.

The fourth key feature of the India-Eurasia velocity field is the observation of widespread dilatation at high elevations. As with diffuse deformation, the presence of widespread dilation is hard to reconcile with microplate/block models without allowing internal deformation within the blocks. To produce such dilation with continuum models is possible but implies a chance in the balance of forces within the system (e.g., England & Houseman, 1989).

In addition to these key features, England and Molnar (2005) argued that a discriminatory test between microplate/block models is the orientation of contours of velocity magnitude. If microplates/blocks are large, the velocity magnitudes within the blocks should be constant and changes in the velocity should only occur along the boundaries—for horizontally translating blocks, the contours of velocity magnitude should be parallel to the velocity direction. In contrast, continuum models would predict that the contours of velocity magnitude should be approximately perpendicular to the orientation of the velocity vectors. In Figure S7 we show the contours of velocity magnitude. In general, the contours are approximately perpendicular to the velocity vectors.

In summary, neither block nor continuum models in their purest forms can explain the key observations of deformation that are observed in the GPS velocity field for the India-Eurasia collision. The pattern of deformation observed is inconsistent with the deformation we would expect from a few large blocks that act in a way that is analogous to plate tectonics. Of course, we could explain the kinematics of all of the GPS perfectly with a sufficiently large number of blocks moving independently, but such a model would have little practical use. Furthermore, we will never know where all the block boundaries are, and hence, using such models to inform seismic hazard assessments can be dangerous—leading to an underestimation of the likelihood of earthquakes occurring on unknown faults away from block boundaries. Continuum models also struggle to explain aspects of the deformation field and likely require variations in material properties in space and the evolution of material properties in time to explain the observations. Nevertheless, they are appealing in that they offer the potential to explain the deformation observed over large regions with relatively few parameters and the ability to investigate the impact of different rheological properties of the lithosphere. Further work is required to create a self-consistent dynamic model that matches the key features observed in real deformation field.

4.4. Implications for Seismic Hazard

Our strain rate field (second invariant) shows elevated strain rates of $>$10 nanostrain/yr for about half of our study region (Figure 11). If we assume that this strain represents the accumulation of elastic strain energy in the upper crust, then taking a 100 $\times$ 100 km area with a typical seismogenic thickness of 15 km (Wright et al., 2013) for every 100 years, we would expect earthquakes with a cumulative seismic moment of at least 10^{19} Nm (Kostrov, 1974), equivalent to a single earthquake with M_w 6.6. Even in about one third of the study region where present-day strain rates can be constrained to be less than 5 nanostrain/yr (Figure 11), we cannot rule out significant seismicity and nowhere should be considered risk free.

Some localized regions display significantly higher strain rates suggesting a higher local hazard, often associated with some of the major faults. Our strain rate fields show that apparently high strain rates mainly lie along the major structures in the Himalaya, the boundaries of the Tien Shan, and the Sagaing, Altyn Tagh, Kunlun, and Xianshuihe-Xiaojiang Faults (Figures 4, 5a, and 5c). A few regions are worthy of special comment.

First, the central Sagaing Fault has the highest strain rates observed in our entire study area. It has been suggested as a seismic gap (Hurukawa & Maung Maung, 2011), where the last great earthquake might be the 1839 M_w 7.8 Ava event. If so, the accumulated strain energy since this date, assuming constant rates in time, would be able to generate a M_w 7.6 earthquake (Wang et al., 2014).

Second, the Xidatan-Dongdatan segment of the Kunlun Fault completely lies in the high-strain region at ~92–96.5°E between the 1937 M_w 7.8 Tuosuo Lake (97.8°E, 35.4°N) and the 2001 M_w 7.8 Kokoxili (90.5°E, 35.9°N) earthquakes. Although no surface-rupturing earthquakes have been recorded in the instrumental period, Van Der Woerd et al. (2002) suggested that ~M 8.0 earthquakes recur here every ~800–1000 years. Moreover, the preceding earthquakes in the Kunlun Fault might push this segment closer to failure due to stress loading (Xie et al., 2014; Xiong et al., 2010).

Third, high strain rates occur along the whole Xianshuihe-Xiaojiang fault system, where previous studies have identified four seismic gaps (Shan et al., 2013; Wen et al., 2008). The recent 2014 M_w 5.9 Kangding earthquake struck the Kangding-Daofu gap; however, the released strain energy was far less than that accumulated (Jiang et al., 2015). Therefore, the seismic risk is still high in Kangding-Daofu.

In addition, a seismic gap named Tianzhu has been identified in the Haiyuan Fault, located between the 1920 M 8.6 Haiyuan and the 1927 M 8–8.3 Gulang earthquakes (Gaudemer et al., 1995). It has remained unbroken for ~1000 years (Liu-Zeng et al., 2007), except for some moderate events such as the 2016 M_w 5.9 Menyuan earthquake (Wang, Liu-Zeng, et al., 2017). Our data show deformation consistent with elastic strain accumulation in this region (profile HY1 in Figure 7e); the accumulated slip deficit in the Tianzhu gap since ~1000 is now about 4.3 m. This is within 1 sigma error of the ~5 m coseismic slip of the Haiyuan earthquake from the recent LiDAR study by Ren et al. (2015).

Recent studies have suggested that geodetic strain rates can be used to supplement seismicity catalogues when estimating seismic hazard (e.g., Bird et al., 2010, 2015; Bird & Kreemer, 2015). High-resolution strain data of the type we present here are a fundamental requirement for such hazard models.

5. Conclusions

We present the most complete, accurate, and up-to-date interseismic GPS velocity field for the India-Eurasia collision zone by combining 1556 stations from the CMONOC-I/II projects with 1020 stations compiled by Kreemer et al. (2014).

We use the velocity field to update geodetic estimates of slip rates of the major structures in the region, compare those for the major Tibetan strike-slip faults against available geological estimates, critically assess any apparent discrepancies, and conclude that there is a good correspondence between geological and geodetic slip rates and that any remaining discrepancies likely reflect the uncertainties in the two methods. We note variations in the slip rates along the eastern Altyn Tagh, eastern Kunlun, and Karakoram Faults, which may provide a useful test for models of along-strike fault propagation.

We extract the key features of our new velocity field: there are several large undeforming regions within the India-Eurasia collision zone; some major faults are visible in the velocity field due to strain concentrations; there are regions of diffuse deformation; and the high-elevation regions of Tibet are dilating. We test existing deformation models for the dynamics of the India-Eurasia collision, and find that neither block nor continuum models can usefully explain the observations without substantial modification and suggest that a new generation of models is required.

We find obviously higher strain rates with respect to the surroundings at the seismic gaps in the Sagaing, Kunlun, and Xianshuihe-Xiaojiang Faults, which may suffer from great earthquakes (possibly $M_w \geq 7.5$) in the future. Two thirds of the study region have a measurably elevated strain rate of >5 nanostrain/yr and nowhere should be considered free of the risk of significant earthquakes.

Acknowledgments
All data supporting the conclusions of this paper are available in the supporting information section and uploaded separately as a file named "ds01.txt" (see caption for Data Set S1 in the supporting information for instructions). We are grateful to all the people who contribute to CMONOC-I/II. We appreciate the generosity of Corné Kreemer (University of Nevada, Reno) in sharing his GPS velocities. We thank Peter Bird and David Jackson (University of California, Los Angeles); Eric Kirby (Oregon State University); and Weijun Gan, Yongge Wan, and Shiming Liang (China Earthquake Administration) for helpful discussions. This work was supported by the NSFC projects (41372221, 41374034, 41672205) and NERC through the Centre for the Observation and Modeling of Earthquakes, Volcanoes, and Tectonics (COMET).

References

Ader, T., Avouac, J.-P., Liu-Zeng, J., Lyon-Caen, H., Bollinger, L., Galetzka, J., … Flouzat, M. (2012). Convergence rate across the Nepal Himalaya and interseismic coupling on the Main Himalayan Thrust: Implications for seismic hazard. *Journal of Geophysical Research*, *117*, B04403. https://doi.org/10.1029/2011JB009071

Allen, C. R., Gillespie, A. R., Yuan, H., Sieh, K. E., Buchun, Z., & Chengnan, Z. (1984). Red River and associated faults, Yunnan Province, China: Quaternary geology, slip rate and seismic hazard. *Geological Society of America Bulletin*, *95*, 686–700. https://doi.org/10.1130/0016-7606(1984)95%3C686:RRAAFY%3E2.0.CO;2

Allen, C. R., Zhuoli, L., Hong, Q., Xueze, W., Huawei, Z., & Weishi, H. (1991). Field study of a highly active fault zone: The Xianshuihe Fault of southwestern China. *Geological Society of America Bulletin*, *103*, 1178–1199. https://doi.org/10.1130/0016-7606(1991)103%3C1178:FSOAHA%3E2.3.CO;2

Armijo, R., Tapponnier, P., Mercier, J. L., & Han, T.-L. (1986). Quaternary extension in southern Tibet: Field observations and tectonic implications. *Journal of Geophysical Research: Solid Earth*, *91*, 13,803–13,872. https://doi.org/10.1029/JB091iB14p13803

Avouac, J. P., & Tapponnier, P. (1993). Kinematic model of active deformation in central Asia. *Geophysical Research Letters*, *20*, 895–898. https://doi.org/10.1029/93GL00128

Banerjee, P., & Bürgmann, R. (2002). Convergence across the northwest Himalaya from GPS measurements. *Geophysical Research Letters*, *29*(13), 1652. https://doi.org/10.1029/2002GL015184

Banerjee, P., Burgmann, R., Nagarajan, B., & Apel, E. (2008). Intraplate deformation of the Indian subcontinent. *Geophysical Research Letters*, *35*, L18301. https://doi.org/10.1029/2008GL035468

Bendick, R., Bilham, R., Freymueller, J., Larson, K., & Yin, G. (2000). Geodetic evidence for a low slip rate in the Altyn Tagh Fault system. *Nature*, *386*, 61–64.

Bettinelli, P., Avouac, J.-P., Flouzat, M., Jouanne, F., Bollinger, L., Willis, P., & Chitrakar, G. R. (2006). Plate motion of India and interseismic strain in the Nepal Himalaya from GPS and DORIS measurements. *Journal of Geodesy*, *80*, 567–589.

Bilham, R., Larson, K., & Freymueller, J. (1997). GPS measurements of present-day convergence across the Nepal Himalaya. *Nature*, *386*, 61–64. https://doi.org/10.1038/386061a0

Bird, P., & Kreemer, C. (2015). Revised tectonic forecast of global shallow seismicity based on version 2.1 of the Global Strain Rate Map. *Bulletin of the Seismological Society of America*, *105*(1), 152–166. https://doi.org/10.1785/0120140129

Bird, P., Jackson, D. D., Kagan, Y. Y., Kreemer, C., & Stein, R. S. (2015). GEAR1: A global earthquake activity rate model constructed from geodetic strain rates and smoothed seismicity. *Bulletin of the Seismological Society of America*, *105*(5), 2538–2554. https://doi.org/10.1785/0120150058

Bird, P., Kreemer, C., & Holt, W. E. (2010). A long-term forecast of shallow seismicity based on the Global Strain Rate Map. *Seismological Research Letters*, *81*(2), 184–194. https://doi.org/10.1785/gssrl.81.2.184

Boehm, J., Niell, A., Tregoning, P., & Schuh, H. (2006). Global Mapping Function (GMF): A new empirical mapping function based on numerical weather model data. *Geophysical Research Letters*, *33*, L07304. https://doi.org/10.1029/2005GL025546

Brown, E. T., Bendick, R., Bourlès, D. L., Gaur, V., Molnar, P., Raisbeck, G. M., & Yiou, F. (2002). Slip rates of the Karakorum Fault, Ladakh, India, determined using cosmic ray exposure dating of debris flows and moraines. *Journal of Geophysical Research*, *107*(B9), 2192. https://doi.org/10.1029/2000JB000100

Burchfiel, B. C., Zhang, P., Wang, Y., Zhang, W., Song, F., Deng, Q., … Royden, L. (1991). Geology of Haiyuan fault zone, Ningxia-Hui Autonomous Region, China, and its relation to the evolution of the northeastern margin of the Tibetan Plateau. *Tectonics*, *10*(6), 1091–1110. https://doi.org/10.1029/90TC02685

Burchfiel, B. C., Zhiliang, C., Yupinc, L., & Royden, L. H. (1995). Tectonics of the Longmen Shan and adjacent regions, central China. *International Geology Review*, *37*(8), 661–735. https://doi.org/10.1080/00206819509465424

Cavalié, O., Lasserre, C., Doin, M.-P., Peltzer, G., Sun, J., Xu, X., & Shenb, Z.-K. (2008). Measurement of interseismic strain across the Haiyuan Fault (Gansu, China), by InSAR. *Earth and Planetary Science Letters*, *275*(3–4), 246–257. https://doi.org/10.1016/j.epsl.2008.07.057

Chen, Z., Burchfiel, B. C., Liu, Y., King, R. W., Royden, L. H., Tang, W., … Zhang, X. (2000). Global Positioning System measurements from eastern Tibet and their implications for India/Eurasia intercontinental deformation. *Journal of Geophysical Research*, *105*, 16,215–16,227. https://doi.org/10.1029/2000JB900092

Chen, Q., Freymueller, J. T., Wang, Q., Yang, Z., Xu, C., & Liu, J. (2004). A deforming block model for the present-day tectonics of Tibet. *Journal of Geophysical Research*, *109*, B01403. https://doi.org/10.1029/2002JB002151

Chen, Y., Li, S. H., Sun, J. M., & Fu, B. H. (2013). OSL dating of offset streams across the Altyn Tagh Fault: Channel deflection, loess deposition and implication for the slip rate. *Tectonophysics*, *594*(3), 182–194. https://doi.org/10.1016/j.tecto.2013.04.002

Chevalier, M.-L., Ryerson, F. J., Tapponnier, P., Finkel, R. C., Van Der Woerd, J., Li, H., & Liu, Q. (2005). Slip-rate measurements on the Karakorum Fault may imply secular variations in fault motion. *Science*, *237*, 411–414.

Chevalier, M.-L., Van der Woerd, J., Tapponnier, P., Li, H., Ryerson, F. J., & Finkel, R. C. (2015). Late Quaternary slip-rate along the central Bangong-Chaxikang segment of the Karakorum Fault, western Tibet. *Geological Society of America Bulletin*, *128*(1/2), 284–314. https://doi.org/10.1130/B31269.1

Copley, A., Avouac, J.-P., & Wernicke, B. P. (2011). Evidence for mechanical coupling and strong Indian lower crust beneath southern Tibet. *Nature*, *472*(7341), 79–81. https://doi.org/10.1038/nature09926

Cowgill, E. (2007). Impact of riser reconstructions on estimation of secular variation in rates of strike–slip faulting: Revisiting the Cherchen River site along the Altyn Tagh Fault, NW China. *Earth and Planetary Science Letters*, *254*(3), 239–255.

Cowgill, E., Gold, R. D., Chen, X., Wang, X. F., Ramón Arrowsmith, J., & Southon, J. (2009). Low Quaternary slip rate reconciles geodetic and geologic rates along the Altyn Tagh Fault, northwestern Tibet. *Geology*, *37*(7), 647–650. https://doi.org/10.1130/G25623A.1

Daout, S., Jolivet, R., Lasserre, C., Doin, M.-P., Barbot, S., Tapponnier, P., … Sun, J. (2016). Along-strike variations of the partitioning of convergence across the Haiyuan fault system detected by InSAR. *Geophysical Journal International*, *205*, 536–547. https://doi.org/10.1093/gji/ggw028

Dayem, K. E., Houseman, G. A., & Molnar, P. (2009). Localization of shear along a lithospheric strength discontinuity: Application of a continuous deformation model to the boundary between Tibet and the Tarim Basin. *Tectonics*, *28*, TC3002. https://doi.org/10.1029/2008TC002264

De Bresser, J., Ter Heege, J., & Spiers, C. (2001). Grain size reduction by dynamic recrystallization: Can it result in major rheological weakening? *International Journal of Earth Sciences*, *90*(1), 28–45. https://doi.org/10.1007/s005310000149

Deng, Q., Zhang, P., Ran, Y., Yang, X., Min, W., & Chu, Q. (2003). Basic characteristics of active tectonics of China. *Science in China, Series D: Earth Sciences*, *46*, 356–372.

Densmore, A. L., Ellis, M. A., Li, Y., Zhou, R., Hancock, G. S., & Richardson, N. (2007). Active tectonics of the Beichuan and Pengguan Faults at the eastern margin of the Tibetan Plateau. *Tectonics*, *26*, TC4005. https://doi.org/10.1029/2006TC001987

Duvall, A. R., & Clark, M. K. (2010). Dissipation of fast strike-slip faulting within and beyond northeastern Tibet. *Geology*, *38*(3), 223–226. https://doi.org/10.1130/G30711.1

Elliott, J., Walters, R. J., England, P. C., Jackson, J. A., Li, Z., & Parsons, B. (2010). Extension on the Tibetan Plateau: Recent normal faulting measured by InSAR and body wave seismology. *Geophysical Journal International*, *183*(2), 503–535. https://doi.org/10.1111/j.1365-246X.2010.04754.x

Elliott, J., Walters, R. J., & Wright, T. J. (2016). The role of space-based observation in understanding and responding to active tectonics and earthquakes. *Nature Communications*, *7*, 13844. https://doi.org/10.1038/ncomms13844

Elliott, J. R., Biggs, J., Parsons, B., & Wright, T. J. (2008). InSAR slip rate determination on the Altyn Tagh Fault, northern Tibet, in the presence of topographically correlated atmospheric delays. *Geophysical Research Letters*, *35*, L12309. https://doi.org/10.1029/2008GL033659

England, P., & Houseman, G. (1986). Finite strain calculations of continental deformation: 2. Comparison with the India-Asia collision zone. *Journal of Geophysical Research*, *91*(B3), 3664–3676. https://doi.org/10.1029/JB091iB03p03664

England, P., & Houseman, G. (1989). Extension during continental convergence, with application to the Tibetan Plateau. *Journal of Geophysical Research*, *94*(B12), 17,561–17,579. https://doi.org/10.1029/JB094iB12p17561

England, P., & McKenzie, D. (1982). A thin viscous sheet model for continental deformation. *Geophysical Journal International*, *70*(2), 295–321.

England, P., & Molnar, P. (2005). Late Quaternary to decadal velocity fields in Asia. *Journal of Geophysical Research*, *110*, B12401. https://doi.org/10.1029/2004JB003541

Fielding, E., Isacks, B., Barazangi, M., & Duncan, C. (1994). How flat is Tibet? *Geology*, *22*(2), 163–167. https://doi.org/10.1130/0091-7613(1994)022%3C0163:HFIT%3E2.3.CO;2

Flesch, L. M., John Haines, A., & Holt, W. E. (2001). Dynamics of the India-Eurasia collision zone. *Journal of Geophysical Research*, *106*, 16,435–16,460. https://doi.org/10.1029/2001JB000208

Floyd, M., Billiris, H., Paradissis, D., Veis, G., Avallone, A., Briole, P., … England, P. C. (2010). A new velocity field for Greece: Implications for the kinematics and dynamics of the Aegean. *Journal of Geophysical Research*, *115*, B10403. https://doi.org/10.1029/2009JB007040

Freymueller, J. T. (2011). GPS—Tectonic geodesy. In H. Gupta (Ed.), *Encyclopedia of Solid Earth Geophysics* (pp. 431–449). Netherlands: Springer. https://doi.org/10.1007/978-90-481-8702-7_77

Gan, W. J., Zhang, P., Shen, Z.-K., Niu, Z., Wang, M., Wan, Y., … Cheng, J. (2007). Present-day crustal motion within the Tibetan Plateau inferred from GPS measurements. *Journal of Geophysical Research*, *112*, B08416. https://doi.org/10.1029/2005JB004120

Garthwaite, M. C., Wang, H., & Wright, T. J. (2013). Broad-scale interseismic deformation and fault slip rates in the central Tibetan Plateau observed using InSAR. *Journal of Geophysical Research: Solid Earth*, *118*, 5071–5083. https://doi.org/10.1002/jgrb.50348

Gaudemer, Y., Tapponnier, P., Meyer, B., Peltzer, G., Shunmin, G., Zhitai, C., … Cifuentes, I. (1995). Partitioning of crustal slip between linked, active faults in the eastern Qilian Shan, and evidence for a major seismic gap, the Tianzhu Gap, on the western Haiyuan Fault, Gansu (China). *Geophysical Journal International*, *120*(3), 599–645. https://doi.org/10.1111/j.1365-246X.1995.tb01842.x

Ge, W.-P., Molnar, P., Shen, Z.-K., & Li, Q. (2015). Present-day crustal thinning in the southern and northern Tibetan Plateau revealed by GPS measurements. *Geophysical Research Letters*, *42*, 5227–5235. https://doi.org/10.1002/2015GL064347

Gendt, G., Dick, G., Reigber, C., Tomassini, M., Liu, Y., & Ramatschi, M. (2003). Demonstration of NRT GPS water vapor monitoring for numerical weather prediction in Germany. *Journal of the Meteorological Society of Japan*, *82*, 360–370.

Gold, R. D., & Cowgill, E. (2011). Deriving fault-slip histories to test for secular variation in slip, with examples from the Kunlun and Awatere Faults. *Earth and Planetary Science Letters*, *301*, 52–64.

Gold, R. D., Cowgill, E., Arrowsmith, J. R., & Friedrich, A. M. (2017). Pulsed strain release on the Altyn Tagh Fault, northwest china. *Earth and Planetary Science Letters*, *459*, 291–300.

Hammond, W. C., Blewitt, G., & Kreemer, C. (2011). Block modeling of crustal deformation of the northern Walker Lane and Basin and Range from GPS velocities. *Journal of Geophysical Research*, *116*, B04402. https://doi.org/10.1029/2010JB007817

Hao, M., Wang, Q., Shen, Z., Cui, D., Ji, L., Li, Y., & Qin, S. (2014). Present day crustal vertical movement inferred from precise leveling data in eastern margin of Tibetan Plateau. *Tectonophysics*, *632*, 281–292.

Harkins, N., & Kirby, E. (2008). Fluvial terrace riser degradation and determination of slip rates on strike-slip faults: An example from the Kunlun Fault, China. *Geophysical Research Letters*, *35*, L05406. https://doi.org/10.1029/2007GL033073

Harkins, N., Kirby, E., Shi, X., Wang, E., Burbank, D., & Chun, F. (2010). Millennial slip rates along the eastern Kunlun Fault: Implications for the dynamics of intracontinental deformation in Asia. *Lithosphere*, *2*, 247–266.

He, J., Vernant, P., Chéry, J., Wang, W., Lu, S., Ku, W., … Bilham, R. (2013). Nailing down the slip rate of the Altyn Tagh Fault. *Geophysical Research Letters*, *40*, 5382–5386. https://doi.org/10.1002/2013GL057497

Hetzel, R., Niedermann, S., Tao, M., Kubik, P. W., Ivy-Ochs, S., Gao, B., & Strecker, M. R. (2002). Low slip rates and long-term preservation of geomorphic features in central Asia. *Nature*, *417*, 428–432.

Houseman, G., & England, P. (2017). The stability of Tibetan mantle lithosphere, paper presented at EGU General Assembly Conference Abstracts.

Hu, X., Garzanti, E., Wang, J., Huang, W., An, W., & Webb, A. (2016). The timing of India-Asia collision onset—Facts, theories, controversies. *Earth-Science Reviews*, *160*, 264–299.

Huang, W., Gao, W., & Ding, G. (1996). Neogene volcanism and Holocene earthquakes in the Tanlu Fault zone, eastern China. *Tectonophysics*, *260*(4), 259–270.

Hurukawa, N., & Maung Maung, P. (2011). Two seismic gaps on the Sagaing Fault, Myanmar, derived from relocation of historical earthquakes since 1918. *Geophysical Research Letters*, *38*, L01310. https://doi.org/10.1029/2010GL046099

Jade, S., Bhatt, B. C., Yang, Z., Bendick, R., Gaur, V. K., Molnar, P., … Kumar, D. (2004). GPS measurements from the Ladakh Himalaya, India: Preliminary tests of plate-like or continuous deformation in Tibet. *Geological Society of America Bulletin*, *116*, 1385–1391. https://doi.org/10.1130/B25357.1

Jiang, G., Wen, Y., Liu, Y., Xu, X., Fang, L., Chen, G., … Xu, C. (2015). Joint analysis of the 2014 Kangding, southwest China, earthquake sequence with seismicity relocation and InSAR inversion. *Geophysical Research Letters*, *42*, 3273–3281. https://doi.org/10.1002/2015GL063750

Jolivet, R., Cattin, R., Chamot-Rooke, N., Lasserre, C., & Peltzer, G. (2008). Thin-plate modeling of interseismic deformation and asymmetry across the Altyn Tagh fault zone. *Geophysical Research Letters*, *35*, L02309. https://doi.org/10.1029/2007GL031511

Jolivet, R., Lasserre, C., Doin, M.-P., Guillaso, S., Peltzer, G., Dailu, R., … Xu, X. (2012). Shallow creep on the Haiyuan Fault (Gansu, China) revealed by SAR interferometry. *Journal of Geophysical Research*, *117*, B06401. https://doi.org/10.1029/2011JB008732

Jolivet, R., Candela, T., Lasserre, C., Renard, F., Klinger, Y., & Doin, M.-P. (2015). The burst-like behavior of aseismic slip on a rough fault: The creeping section of the Haiyuan Fault, China. *Bulletin of the Seismological Society of America*, *105*(1), 480–488.

Kidd, W. S. F., & Molnar, P. (1988). Quaternary and active faulting observed on the 1985 Academia Sinica-Royal Society Geotraverse of Tibet. *Philosophical Transactions of the Royal Society of London*, *327*, 337–363.

King, R. W., & Bock, Y. (1995). Documentation of the GAMIT GPS analysis software, version 9.3. Cambridge, MA: Massachusetts Institute of Technology.

King, R. W., Shen, F., Clark Burchfiel, B., Royden, L. H., Wang, E., & Chen, Z. (1997). Geodetic measurement of crustal motion in southwest China. *Geology*, *25*, 179–182. https://doi.org/10.1130/0091-7613(1997)025%3C0179:GMOCMI%3E2.3.CO;2

Kirby, S. H. (1985). Rock mechanics observations pertinent to the rheology of the continental lithosphere and the localization of strain along shear zones. *Tectonophysics*, *119*(1), 1–27.

Kirby, E., & Harkins, N. (2013). Distributed deformation around the eastern tip of the Kunlun Fault. *International Journal of Earth Sciences*, *102*, 1759–1772.

Kirby, E., Harkins, N., Wang, E., Shi, X., Fan, C., & Burbank, D. (2007). Slip rate gradients along the eastern Kunlun Fault. *Tectonics*, *26*, TC2010. https://doi.org/10.1029/2006TC002033

Kostrov, B. V. (1974). Seismic moment and energy of earthquakes and seismic flow of rock [Engl. Translation]. *Izvestiya of the Academy of Sciences of the USSR, Physics of the Solid Earthlzvestiya*, *1*, 23–40.
Kreemer, C., Blewitt, G., & Klein, E. C. (2014). A geodetic plate motion and Global Strain Rate Model. *Geochemistry, Geophysics, Geosystems*, *15*, 3849–3889. https://doi.org/10.1002/2014GC005407
Kundu, B., Yadav, R. K., Bali, B. S., Chowdhury, S., & Gahalaut, V. K. (2014). Oblique convergence and slip partitioning in the NW Himalaya: Implications from GPS measurements. *Tectonics*, *33*, 2013–2024. https://doi.org/10.1002/2014TC003633
Langbein, J. (2012). Estimating rate uncertainty with maximum likelihood: Differences between power-law and Flicker-random-walk models. *Journal of Geodesy*, *86*(9), 775–783. https://doi.org/10.1007/s00190-012-0556-5
Larson, K. M., Bürgmann, R., Bilham, R., & Freymueller, J. T. (1999). Kinematics of the India-Eurasia collision zone from GPS measurements. *Journal of Geophysical Research*, *104*, 1077–1093.
Lasserre, C., Gaudemer, Y., Tapponnier, P., Meriaux, A.-S., Van der Woerd, J., Daoyan, Y., … Caffee, M. W. (2002). Fast late Pleistocene slip rate on the Leng Long Ling segment of the Haiyuan Fault, Qinghai, China. *Journal of Geophysical Research*, *107*(B11), 2276. https://doi.org/10.1029/2000JB000060
Lasserre, C. P., Morel, P.-H., Gaudemer, Y., Tapponnier, P., Ryerson, F. J., King, G. C. P., … Yuan, D. (1999). Postglacial left slip rate and past occurrence of $M \geq 8$ earthquakes on the western Haiyuan Fault, Gansu, China. *Journal of Geophysical Research*, *104*(B8), 17,633–17,651. https://doi.org/10.1029/1998JB900082
Lechmann, S. M., May, D. A., Kaus, B. J. P., & Schmalholz, S. M. (2011). Comparing thin-sheet models with 3-D multilayer models for continental collision. *Geophysical Journal International*, *187*(1), 10–33.
Li, C., Zhang, P.-z., Yin, J., & Min, W. (2009). Late Quaternary left-lateral slip rate of the Haiyuan Fault, northeastern margin of the Tibetan Plateau. *Tectonics*, *28*, TC5010. https://doi.org/10.1029/2008TC002302
Li, H., Van der Woerd, J., Tapponnier, P., Klinger, Y., Xuexiang, Q., Jingsui, Y., & Yintang, Z. (2005). Slip rate on the Kunlun Fault at Hongshui Gou, and recurrence time of great events comparable to the 14/11/2001, M_w ~7.9 Kokoxili earthquake. *Earth and Planetary Science Letters*, *237*, 285–299.
Li, H., Van der Woerd, J., Sun, Z., Si, J., Tapponnier, P., Pan, J., … Chevalier, M.-L. (2012). Co-seismic and cumulative offsets of the recent earthquakes along the Karakax left-lateral strike-slip fault in western Tibet. *Gondwana Research*, *21*, 64–87.
Li, Q., You, X. Z., Yang, S. M., Du, R. L., Qiao, X. J., Zou, R., & Wang, Q. (2012). A precise velocity field of tectonic deformation in China as inferred from intensive GPS observations. *Science in China Series D Earth Sciences*, *55*(5), 695–698.
Li, Y., Gao, M., & Wu, Q. (2014). Crustal thickness map of the Chinese mainland from teleseismic receiver functions. *Tectonophysics*, *611*, 51–60.
Li, H., Chevalier, M. L., Pan, J., Sun, Z., van der Woerd, J., Liu, D., & Si, J. (2016). Late Quaternary characteristic slip and slip-rate along the Karakax Fault, (western Altyn Tagh Fault), Tibet, AGU Fall Meeting Abstracts.
Liang, S., Gan, W., Shen, C., Xiao, G., Liu, J., Chen, W., … Zhou, D. (2013). Three-dimensional velocity field of present-day crustal motion of the Tibetan Plateau derived from GPS measurements. *Journal of Geophysical Research: Solid Earth*, *118*, 5722–5732. https://doi.org/10.1002/2013JB010503
Liang, X., Chen, Y., Tian, X., Chen, Y. J., Ni, J., Gallegos, A., … Teng, J. (2016). 3D imaging of subducting and fragmenting Indian continental lithosphere beneath southern and central Tibet using body-wave finite-frequency tomography. *Earth and Planetary Science Letters*, *443*, 162–175.
Lin, A., & Guo, J. (2008). Nonuniform slip rate and millennial recurrence interval of large earthquakes along the eastern segment of the Kunlun Fault, northern Tibet. *Bulletin of the Seismological Society of America*, *98*, 2866–2878.
Liu, Q. (1993). Paléoclimat et contraintes chronologiques sur les mouvements récent dans l'Ouest du Tibet: Failles du Karakorum et de Longmu Co-Gozha Co, lacs en pull-apart de Longmu Co et de Sumxi Co, (PhD thesis). Univ. Paris VII, Paris.
Liu-Zeng, J., Klinger, Y., Xu, X., Lasserre, C., Chen, G., Chen, W., … Zhang, B. (2007). Millennial recurrence of large earthquakes on the Haiyuan Fault near Songshan, Gansu Province, China. *Bulletin of the Seismological Society of America*, *97*, 14–34. https://doi.org/10.1785/0120050118
Loveless, J. P., & Meade, B. J. (2011). Partitioning of localized and diffuse deformation in the Tibetan Plateau from joint inversions of geologic and geodetic observations. *Earth and Planetary Science Letters*, *303*, 11–24. https://doi.org/10.1016/j.epsl.2010.12.014
Lyard, F., Lefevre, F., Letellier, T., & Francis, O. (2006). Modelling the global ocean tides: Modern insights from FES2004. *Ocean Dynamics*, *56*(5–6), 394–415. https://doi.org/10.1007/s10236-006-0086-x
McCaffrey, R. (2002). Crustal block rotations and plate coupling. In S. Stein, & J. Freymueller (Eds.), *Plate Boundary Zones, Geodynamics Series* (Vol. 30, pp. 101–122). Washington, DC: American Geophysical Union.
McKenzie, D. P., & Parker, R. L. (1967). The North Pacific: An example of tectonics on a sphere. *Nature*, *216*(5122), 1276–1280.
McKenzie, D., & Priestley, K. (2008). The influence of lithospheric thickness variations on continental evolution. *Lithos*, *102*(1), 1–11.
Meade, B. J., Klinger, Y., & Hetland, E. A. (2013). Inference of multiple earthquake-cycle relaxation timescales from irregular geodetic sampling of interseismic deformation. *Bulletin of the Seismological Society of America*, *103*(5), 2824–2835.
Mériaux, A.-S., Ryerson, F. J., Tapponnier, P., Van der Woerd, J., Finkel, R. C., & Xu, X. (2004). Rapid slip along the central Altyn Tagh Fault: Morphochronologic evidence from Cherchen He and Sulamu Tagh. *Journal of Geophysical Research*, *109*, B06401. https://doi.org/10.1029/2003JB002558
Mériaux, A.-S., Tapponnier, P., Ryerson, F. J., Xiwei, X., King, G., Van der Woerd, J., … Wenbin, C. (2005). The Aksay segment of the northern Altyn Tagh Fault: Tectonic geomorphology, landscape evolution, and Holocene slip rate. *Journal of Geophysical Research*, *110*, B04404. https://doi.org/10.1029/2004JB003210
Meyer, B., Tapponnier, P., Gaudemer, Y., Peltzer, G., Shunmin, G., & Zhitai, C. (1996). Rate of left-lateral movement along the easternmost segment of the Altyn Tagh Fault, east of 96°E (China). *Geophysical Journal International*, *124*(1), 29–44. https://doi.org/10.1111/j.1365-246X.1996.tb06350.x
Molnar, P., & Chen, W.-P. (1983). Focal depths and fault plane solutions of earthquakes under the Tibetan Plateau. *Journal of Geophysical Research*, *88*(B2), 1180–1196. https://doi.org/10.1029/JB088iB02p01180
Molnar, P., England, P., & Martinod, J. (1993). Mantle dynamics, uplift of the Tibetan Plateau, and the Indian monsoon. *Reviews of Geophysics*, *31*(4), 357–396. https://doi.org/10.1029/93RG02030
Molnar, P., & Tapponnier, P. (1975). Cenozoic tectonics of Asia: Effects of a continental collision. *Science*, *189*(4201), 419–426.
Molnar, P., & Tapponnier, P. (1978). Active tectonics of Tibet. *Journal of Geophysical Research*, *83*(B11), 5361–5375. https://doi.org/10.1029/JB083iB11p05361
Murphy, M. A., Yin, A., Kapp, P., Harrison, T. M., Lin, D., & Jinghui, G. (2000). Southward propagation of the Karakorum fault system, southwest Tibet: Timing and magnitude of slip. *Geology*, *28*, 451–454.
Neil, E. A., & Houseman, G. A. (1997). Geodynamics of the Tarim Basin and the Tian Shan in central Asia. *Tectonics*, *16*(4), 571–584. https://doi.org/10.1029/97TC01413

Ni, J., & York, J. E. (1978). Late Cenozoic tectonics of the Tibetan Plateau. *Journal of Geophysical Research*, *83*(B11), 5377–5384. https://doi.org/10.1029/JB083iB11p05377

Peltzer, G., Tapponnier, P., & Armijo, R. (1989). Magnitude of late Quaternary left-lateral displacements along the north edge of Tibet. *Science*, *246*(4935), 1285–1289. https://doi.org/10.1126/science.246.4935.1285

Perrin, C., Manighetti, I., Ampuero, J.-P., Cappa, F., & Gaudemer, Y. (2016). Location of largest earthquake slip and fast rupture controlled by along-strike change in fault structural maturity due to fault growth. *Journal of Geophysical Research: Solid Earth*, *121*, 3666–3685. https://doi.org/10.1002/2015JB012671

Perrin, C., Manighetti, I., & Gaudemer, Y. (2016). Off-fault tip splay networks: A genetic and generic property of faults indicative of their long-term propagation. *Comptes Rendus Geoscience*, *348*, 52–60. https://doi.org/10.1016/j.crte.2015.05.002

Priestley, K., Jackson, J., & McKenzie, D. (2008). Lithospheric structure and deep earthquakes beneath India, the Himalaya and southern Tibet. *Geophysical Journal International*, *172*(1), 345–362.

Rebischung, P., Griffiths, J., Ray, J., Schmid, R., Collilieux, X., & Garayt, B. (2012). IGS08: The IGS realization of ITRF2008. *GPS Solutions*, *16*(4), 483–494. https://doi.org/10.1007/s10291-011-0248-2

Ren, J., Xu, X., Yeats, R. S., & Zhang, S. (2013). Millennial slip rates of the Tazang Fault, the eastern termination of Kunlun Fault: Implications for strain partitioning in eastern Tibet. *Tectonophysics*, *608*, 1180–1200.

Ren, Z., Lin, A., & Rao, G. (2010). Late Pleistocene-Holocene activity of the Zemuhe Fault on the southeastern margin of the Tibetan Plateau. *Tectonophysics*, *495*(3–4), 324–336.

Ren, Z., Zhang, Z., Chen, T., Yan, S., Yin, J., Zhang, P., … Li, C. (2015). Clustering of offsets on the Haiyuan Fault and their relationship to paleoearthquakes. *Geological Society of America Bulletin*, *128*(1). https://doi.org/10.1130/B31155.1

Robinson, A. C. (2009). Evidence against Quaternary slip on the northern Karakorum Fault suggests kinematic reorganization at the western end of the Himalayan-Tibetan orogeny. *Earth and Planetary Science Letters*, *286*, 158–170.

Robinson, A. C., Owen, L. A., Chen, J., Schoenbohm, L. M., Hedrick, K. A., Blisniuk, K., … Mertz-Kraus, R. (2015). No late Quaternary strike-slip motion along the northern Karakoram Fault. *Earth and Planetary Science Letters*, *409*, 290–298. https://doi.org/10.1016/j.epsl.2014.11.011

Rui, X., & Stamps, D. S. (2016). Present-day kinematics of the eastern Tibetan Plateau and Sichuan Basin: Implications for lower crustal rheology. *Journal of Geophysical Research: Solid Earth*, *121*, 3846–3866. https://doi.org/10.1002/2016JB012839

Ryder, I., Bűrgmann, R., & Pollitz, F. (2011). Low crustal relaxation beneath the Tibetan Plateau and Qaidam Basin following the 2001 Kokoxili earthquake. *Geophysical Journal International*, *187*, 613–630. https://doi.org/10.1111/j.1365-246X.2011.05179.x

Ryerson, F. J., Van der Woerd, J., Tapponnier, P., Ryerson, F. J., Finkel, R. C., Lasserre, C., & Xu, X. (1999). Active slip-rates on the Altyn Tagh Fault-Karakax Valley segment: Constraints from surface exposure dating. *Eos, Transactions of the American Geophysical Union*, *80*(46), F1008–F1009.

Saastamoinen, J. (1973). Contributions to the theory of atmospheric refraction—Part II. Refraction corrections in satellite geodesy. *Bulletin Géodésique (1922–1941)*, *47*(1), 13–34. https://doi.org/10.1007/BF02522083

Savage, J. (2000). Viscoelastic-coupling model for the earthquake cycle driven from below. *Journal of Geophysical Research*, *105*(B11), 25,525–25,532. https://doi.org/10.1029/2000JB900276

Savage, J. C., & Burford, R. (1973). Geodetic determination of relative plate motion in central California. *Journal of Geophysical Research*, *95*, 4873–4879. https://doi.org/10.1029/JB078i005p00832

Savage, J. C., Gan, W., & Svarc, J. L. (2001). Strain accumulation and rotation in the Eastern California shear zone. *Journal of Geophysical Research*, *106*(10), 21,995–22,007. https://doi.org/10.1029/2000JB000127

Schmid, R., Steigenberger, P., Gendt, G., Ge, M., & Rothacher, M. (2007). Generation of a consistent absolute phase-center correction model for GPS receiver and satellite antenna. *Journal of Geodesy*, *81*, 781–798.

Shan, B., Xiong, X., Wang, R., Zheng, Y., & Yang, S. (2013). Coulomb stress evolution along Xianshuihe-Xiaojiang fault system since 1713 and its interaction with Wenchuan earthquake, May 12, 2008. *Earth and Planetary Science Letters*, *377-378*(5), 199–210.

Shen, Z.-K., Lü, J., Wang, M., & Bürgmann, R. (2005). Contemporary crustal deformation around the southeast borderland of the Tibetan Plateau. *Journal of Geophysical Research*, *110*, B11409. https://doi.org/10.1029/2004JB003421

Shen, Z.-K., Wang, M., Li, Y., Jackson, D. D., Yin, A., Dong, D., & Fang, P. (2001). Crustal deformation along the Altyn Tagh fault system, western China, from GPS. *Journal of Geophysical Research*, *106*, 30,607–30,621. https://doi.org/10.1029/2001JB000349

Shen, Z.-K., Zhao, C., Yin, A., Li, Y., Jackson, D. D., Fang, P., & Dong, D. (2000). Contemporary crustal deformation in east Asia constrained by Global Positioning System measurements. *Journal of Geophysical Research*, *105*, 5721–5734. https://doi.org/10.1029/1999JB900391

Shen, Z.-K., Sun, J., Zhang, P., Wan, Y., Wang, M., Bürgmann, R., … Wang, Q. (2009). Slip maxima at fault junctions and rupturing of barriers during the 2008 Wenchuan earthquake. *Nature Geoscience*, *2*, 718–724.

Shi, C., M. Li, Q. Zhao, C. Wang, H. Zhang (2015). WHU Analysis Center Technical Report 2014, IGS TECHNICAL REPORT 2014, 81–88.

Takeuchi, C. S., & Fialko, Y. (2012). Dynamic models of interseismic deformation and stress transfer from plate motion to continental transform faults. *Journal of Geophysical Research*, *117*(B5), B05403. https://doi.org/10.1029/2011JB009056

Tapponnier, P., Peltzer, G., Le Dain, A. Y., Armijo, R., & Cobbold, P. (1982). Propagating extrusion tectonics in Asia: New insights from simple experiments with plasticine. *Geology*, *10*, 611–616.

Thatcher, W. (1995). Microplate versus continuum descriptions of active tectonic deformation. *Journal of Geophysical Research*, *100*(B3), 3885–3894. https://doi.org/10.1029/94JB03064

Thatcher, W. (2007). Microplate model for the present-day deformation of Tibet. *Journal of Geophysical Research*, *112*(B1), B01401. https://doi.org/10.1029/2005JB004244

Thatcher, W. (2009). How the continents deform: The evidence from tectonic geodesy. *Annual Review of Earth and Planetary Sciences*, *37*, 237–262.

Thatcher, W., & England, P. C. (1998). Ductile shear zones beneath strike-slip faults: Implications for the thermomechanics of the San Andreas Fault zone. *Journal of Geophysical Research*, *103*(B1), 891–905. https://doi.org/10.1029/97JB02274

Valli, F., Leloup, P. H., Paquette, J. L., Arnaud, N., Li, H. B., Tapponnier, P., … Maheo, G. (2008). New U-Th/Pb constraints on timing of shearing and long-term slip-rate on the Karakorum Fault. *Tectonics*, *27*, TC5007. https://doi.org/10.1029/2007TC002184

Van Der Woerd, J., Tapponnier, P., Ryerson, F. J., Meriaux, A.-S., Meyer, B., Gaudemer, Y., … Zhiqin, X. (2002). Uniform postglacial slip-rate along the central 600 km of the Kunlun Fault (Tibet), from ^{26}Al, ^{10}Be, and ^{14}C dating of riser offsets, and climatic origin of the regional morphology. *Geophysical Journal International*, *148*, 356–388.

Vernant, P. (2015). What can we learn from 20 years of interseismic GPS measurements across strike-slip faults? *Tectonophysics*, *644-645*, 22–39.

Walters, R. J., England, P. C., & Houseman, G. A. (2017). Constraints from GPS measurements on the dynamics of the zone of convergence between Arabia and Eurasia. *Journal of Geophysical Research: Solid Earth*, *122*(2), 1470–1495. https://doi.org/10.1002/2016JB013370

Wang, Y., Sieh, K., Tun, S. T., Lai, K.-Y., & Myint, T. (2014). Active tectonics and earthquake potential of the Myanmar region. *Journal of Geophysical Research: Solid Earth*, *119*, 3767–3822. https://doi.org/10.1002/2013JB010762

Wang, H., & Wright, T. J. (2012). Satellite geodetic imaging reveals internal deformation of western Tibet. *Geophysical Research Letters*, *39*, L07303. https://doi.org/10.1029/2012GL051222

Wang, H., Liu-Zeng, J., Ng, A. H.-M., Ged, L., Javed, F., Long, F., … Shao, Z. (2017). Sentinel-1 observations of the 2016 Menyuan earthquake: A buried reverse event linked to the left-lateral Haiyuan Fault. *International Journal of Applied Earth Observation and Geoinformation*, *61*, 14–21.

Wang, H., Wright, T. J., & Biggs, J. (2009). Interseismic slip rate of the northwestern Xianshuihe Fault from InSAR data. *Geophysical Research Letters*, *36*, L03302. https://doi.org/10.1029/2008GL036560

Wang, S., Wang, E., Fang, X., & Lai, Q. (2011). U-Pb SHRIMP and $^{40}Ar/^{39}Ar$ ages constrain the deformation history of the Karakoram fault zone (KFZ), SW Tibet. *Tectonophysics*, *509*, 208–217.

Wang, Q., Zhang, P.-Z., Freymueller, J. T., Bilham, R., Larson, K. M., Lai, X., … Chen, Q. (2001). Present-day crustal deformation in China constrained by Global Positioning System measurements. *Science*, *294*, 574–577.

Wang, W., Qiao, X., Yang, S., & Wang, D. (2017). Present-day velocity field and block kinematics of Tibetan Plateau from GPS measurements. *Geophysical Journal International*, *208*, 1088–1102.

Washburn, Z., Arrowsmith, J. R., Forman, S. L., Cowgill, E., Xiaofeng, W., Yueqiao, Z., & Zhengle, C. (2001). Late Holocene earthquake history of the central Altyn Tagh Fault, China. *Geology*, *29*, 1051–1054.

Webb, F. H., & Zumberge, J. F. (1993). An introduce to GIPSY-OASIS II, Jet Propulsion Laboratory user manual, JPL Technical Document D-11088, California Institute of Technology.

Weldon, R., Sieh, K. E., Zhu, O., Han, Y., Yang, J., & Robinson, S. (1994). Slip rate and recurrence interval of earthquakes on the Hong He (Red River) Fault, Yunnan, PRC. Paper presented at International Workshop Seismotectonics and Seismic Hazard in South East Asia, UNESCO, Hanoi.

Wen, X. Z., Han, W., Li, T., Zhou, Y., He, Y., Weldon, R., … Yang, Y. (1996). Slip-rate and recurrence intervals of the Luhuo/Daofu segment of the Xianshuihe Fault, Sichuan, PRC. *Eos, Transactions of the American Geophysical Union*, *77*(46), F693–F694.

Wen, X. Z., Ma, S.-L., Xu, X.-W., & He, Y.-N. (2008). Historical pattern and behavior of earthquake ruptures along the eastern boundary of the Sichuan-Yunan faulted-block, southwestern China. *Physics of the Earth and Planetary Interiors*, *168*, 16–36.

Wright, T. J., Elliott, J. R., Wang, H., & Ryder, I. (2013). Earthquake cycle deformation and the Moho: Implications for the rheology of continental lithosphere. *Tectonophysics*, *609*, 504–523.

Wright, T. J., Parsons, B., England, P. C., & Fielding, E. J. (2004). InSAR observations of low slip rates on the major faults of western Tibet. *Science*, *305*(5681), 236–239. https://doi.org/10.1126/science.1096388

Wu, J. T., Wu, S. C., Hajj, G. A., Bertiger, W. I., & Lichten, S. M. (1993). Effects of antenna orientation on GPS carrier phase. *Manuscripta Geodaetica*, *18*, 91–98.

Xie, C. D., Lei, X., Wu, X., & Hu, X. (2014). Short- and long-term earthquake triggering along the strike-slip Kunlun Fault, China: Insights gained from the M_S 8.1 Kunlun earthquake and other modern large earthquakes. *Tectonophysics*, *617*, 114–125.

Xiong, X., Shan, B., Zheng, Y., & Wang, R. (2010). Stress transfer and its implication for earthquake hazard on the Kunlun Fault, Tibet. *Tectonophysics*, *482*, 216–225.

Xu, X. W., Wang, F., Zheng, R., Chen, W., Ma, W., Yu, G., … Ryerson, F. J. (2005). Late Quaternary sinistral slip rate along the Altyn Tagh Fault and its structural transformational model. *Science in China Series D: Earth Sciences*, *48*, 384–397.

Xu, X. W., Wen, X. Z., Chen, G. H., & Yu, G. H. (2008). Discovery of the Longriba fault zone in eastern Bayan Har Block, China and its tectonic implication. *Science in China Series D: Earth Sciences*, *51*(9), 1209–1223.

Xu, X. W., Wen, X., Zheng, R., Ma, W., Song, F., & Yu, G. (2003). Pattern of latest tectonic motion and its dynamics for active blocks in Sichuan-Yunnan region, China. *Science in China Series D: Earth Sciences*, *46*, 210–226.

Yamasaki, T., Wright, T. J., & Houseman, G. A. (2014). Weak ductile shear zone beneath a major strike-slip fault: Inferences from earthquake cycle model constrained by geodetic observations of the western North Anatolian fault zone. *Journal of Geophysical Research: Solid Earth*, *119*(4), 3678–3699. https://doi.org/10.1002/2013JB010347

Yin, A., Rumelhart, P. E., Butler, R., Cowgill, E., Harrison, T. M., Foster, D. A., … Raza, A. (2002). Tectonic history of the Altyn Tagh Fault system in northern Tibet inferred from Cenozoic sedimentation. *Geological Society of America Bulletin*, *114*, 1257–1295.

Yuan, D. Y., Champagnac, J.-D., Ge, W.-P., Molnar, P., Zhang, P.-Z., Zheng, W.-J., … Liu, X.-W. (2011). Late Quaternary right-lateral slip rates of faults adjacent to the lake Qinghai, northeastern margin of the Tibetan Plateau. *Geological Society of America Bulletin*, *123*(9–10), 2016–2030. https://doi.org/10.1130/B30315.1

Zhang, P. Z. (2013a). Beware of slowly slipping faults. *Nature Geoscience*, *6*, 323–324.

Zhang, P. Z. (2013b). A review on active tectonics and deep crustal processes of the western Sichuan region, eastern margin of the Tibetan Plateau. *Tectonophysics*, *584*, 7–22. https://doi.org/10.1016/j.tecto.2012.02.021

Zhang, P. Z., Burchfiel, B. C., Molnar, P., Zhang, W., Jiao, D., Deng, Q., … Song, F. (1991). Amount and style of late Cenozoic deformation in the Liupan Shan area, Ningxia Autonomous Region, China. *Tectonics*, *10*(6), 1111–1129. https://doi.org/10.1029/90TC02686

Zhang, P. Z., Molnar, P., & Xu, X. (2007). Late Quaternary and present-day rates of slip along the Altyn Tagh Fault, northern margin of the Tibetan Plateau. *Tectonics*, *26*, TC5010. https://doi.org/10.1029/2006TC002014

Zhang, P. Z., Molnar, P., Burchfiel, B. C., Royden, L., Yipeng, W., Qidong, D., … Decheng, J. (1988). Bounds on the Holocene slip rate of the Haiyuan Fault, north-central China. *Quaternary Research*, *30*(2), 151–164.

Zhang, P. Z., Shen, Z., Wang, M., Gan, W., Bürgmann, R., Molnar, P., … Xinzhao, Y. (2004). Continuous deformation of the Tibetan Plateau from Global Positioning System data. *Geology*, *32*(9), 809–812.

Zhang, Y. Q., Mercier, J. L., & Vergély, P. (1998). Extension in the graben systems around the Ordos (China), and its contribution to the extrusion tectonics of south China with respect to Gobi-Mongolia. *Tectonophysics*, *285*(1–2), 41–75.

Zhao, B. (2015). Crustal deformation on the Chinese mainland during 1998–2004 based on GPS data. *Geodesy and Geodynamics*, *6*(1), 7–15.

Zheng, W.-J., Pei-zhen, Z., Wen-gui, H., Dao-yang, Y., Yan-xiu, S., De-wen, Z., … Wei, M. (2013). Transformation of displacement between strike-slip and crustal shortening in the northern margin of the Tibetan Plateau: Evidence from decadal GPS measurements and late Quaternary slip rates on faults. *Tectonophysics*, *584*, 267–280.

Zumberge, J. F., Heflin, M. B., Jefferson, D. C., Watkins, M. M., & Webb, F. H. (1997). Precise point positioning for the efficient and robust analysis of GPS data from large networks. *Journal of Geophysical Research*, *102*(B3), 5005–5017. https://doi.org/10.1029/96JB03860